# Fully implicit, stabilised MPM simulation of large-deformation problems in two-phase elastoplastic geomaterials

Zheng, Xiangcou; Pisanò, Federico; Vardon, Philip J.; Hicks, Michael A.

**DOI**
10.1016/j.compgeo.2022.104771

**Publication date**
2022

**Document Version**
Final published version

**Published in**
Computers and Geotechnics

Computers and Geotechnics 147 (2022) 104771

Contents lists available at ScienceDirect

Computers and Geotechnics

journal homepage: www.elsevier.com/locate/compgeo

Research paper

# Fully implicit, stabilised MPM simulation of large-deformation problems in two-phase elastoplastic geomaterials

Xiangcou Zheng, Federico Pisanò, Philip J. Vardon, Michael A. Hicks *

*Geo-Engineering Section, Faculty of Civil Engineering and Geosciences, Delft University of Technology, Delft, The Netherlands*

ARTICLE INFO

*Keywords:*
$\overline{\text{B}}$ approach
Coupled poromechanics
Implicit time integration
Large deformation
Material point method
Volumetric locking

ABSTRACT

The Material Point Method (MPM) has been gaining increasing popularity as an appropriate approach to the solution of coupled hydro-mechanical problems involving large deformations. This study extends the implicit GIMP-patch method for coupled poroelastic problems recently proposed by Zheng et al. (2021b) to tackle large-deformation problems in (nearly) isochoric elastoplastic geomaterials, particularly by remedying the numerical inaccuracies caused by volumetric locking, such as spurious stress oscillations and an excessively stiff overall response of the system at hand. To overcome these difficulties in two-phase coupled analyses, the $\overline{\text{B}}$ approach of Hughes (1980) is incorporated into an existing version of the implicit GIMP-patch method. Details regarding the formulation and implementation of the proposed method are provided, while several benchmark problems are numerically analysed to evaluate its performance in the presence of elastoplastic behaviour. Particular emphasis is placed on (i) mitigating effective stress oscillations and (ii) solving several two-phase, coupled, large deformation geotechnical problems. The numerical results confirm the suitability of the implicit $\overline{\text{B}}$ GIMP-patch method for the solution of geotechnical problems spanning weak to strong hydro-mechanical coupling and small to large deformations.

## 1. Introduction

The numerical simulation of large-deformation problems in fluid-saturated geomaterials is central to numerous geotechnical applications. In this respect, it has been largely recognised that purely Lagrangian, mesh-based numerical methods are not suitable for large-deformation modelling, as they would usually suffer from the detriments of excessive mesh distortion in terms of numerical accuracy and stability (Lee and Bathe, 1993; Rajendran, 2010). To remedy this issue, it is necessary to resort to specific techniques for re-meshing and variable mapping across a sequence of different spatial discretisations. An alternative approach for mitigating mesh distortion effects is to combine the advantages of both Lagrangian and Eulerian methods, which is the basis of the so-called Material Point Method (MPM). The MPM uses a background mesh for solving relevant governing equations in their discrete form, while material state variables are stored at Material Points (MPs) that can freely move through the background mesh. Based on this idea, the MPM can overcome the inconveniences of mesh distortion and is being increasingly recognised as a suitable approach for large-deformation modelling (Zhang et al., 2007, 2009; Higo et al., 2010; Zabala and Alonso, 2011; Abe et al., 2014; Jassim et al., 2013; Zheng et al., 2013; Bandara and Soga, 2015; Higo et al., 2015; Yerro et al., 2015; Ceccato et al., 2016; Liu et al., 2017; Yang et al., 2017; Yerro et al., 2017; Wang et al., 2018; González Acosta et al., 2019; Lei et al., 2020; Zhao and Choo, 2020; Zheng et al., 2021a; Martinelli and Pisanò, 2022). An overview of different applications of the MPM to geotechnical large-deformation problems can be found in, for instance, Soga et al. (2015). It is well-known that MPM also suffers from many issues due to numerical oscillations in the simulation of large deformations. Some techniques, such as the Generalised Interpolation Material Point (GIMP) method (Bardenhagen and Kober, 2004), the Convected Particle Domain Interpolation (CPDI) method (Sadeghirad et al., 2011), the B-spline Material Point Method (BSMPM) (Steffen et al., 2008), and the Composite Material Point Method (CMPM) (González Acosta et al., 2017, 2020), have been proposed and these have been found to significantly improve the accuracy of MPM.

Given the focus of the present work on fluid-saturated geomaterials, Table 1 summarises the main features of the MPM studies that have been previously devoted to hydro-mechanical large-deformation problems. It should be noted that most of the listed publications build on the $u$–$p$ and $v$–$w$ formulations (where $u$ is the total solid displacement, $p$ is the pore water pressure, and $v$ and $w$ are the velocities of the solid and water phases, respectively). The main difference between these two formulations lies in the relative acceleration of the fluid with

* Corresponding author.
*E-mail address:* M.A.Hicks@tudelft.nl (M.A. Hicks).

https://doi.org/10.1016/j.compgeo.2022.104771
Received 21 January 2022; Received in revised form 30 March 2022; Accepted 15 April 2022
Available online 7 May 2022

**Table 1**
Overview of existing MPM formulations for large-deformation problems in fluid-saturated porous media.

| Reference | Formulation | MP layering | Time integration | Soil model | Pore pressure stabilisation method |
|---|---|---|---|---|---|
| Zhang et al. (2007) | $u$–$U$ | Two-layers | Explicit | Elastic | No stabilisation (or not mentioned) |
| Zhang et al. (2009) | $u$–$p$ | Single-layer | Explicit | Elastic | No stabilisation (or not mentioned) |
| Zabala and Alonso (2011) | $u$–$p$ | Single-layer | Explicit | Mohr–Coulomb | Reduced integration (RI) |
| Abe et al. (2014) | $u$–$p$ | Two-layers | Explicit | Mohr–Coulomb | Reduced integration (RI) |
| Jassim et al. (2013) | $v$–$w$ | Single-layer | Explicit | Mohr–Coulomb | Nodal volumetric strain averaging |
| Zheng et al. (2013) | $u$–$p$ | Single-layer | Explicit | Elastic | No stabilisation (or not mentioned) |
| Bandara and Soga (2015) | $v$–$w$ | Two-layers | Explicit | Mohr–Coulomb | Reduced integration (RI) |
| Martinelli and Rohe (2015) | $v$–$w$ | Two-layers | Explicit | Mohr–Coulomb | No stabilisation (or not mentioned) |
| Ceccato et al. (2016) | $v$–$w$ | Single-layer | Explicit | Modified Cam Clay | Nodal strain averaging + Constant pore pressure in element |
| Liu et al. (2017) | $v$–$w$ | Two-layers | Explicit | Drucker–Prager | No stabilisation (or not mentioned) |
| Tran and Sołowski (2019) | $v$–$w$ | Two-layers | Explicit | Elastic | No stabilisation (or not mentioned) |
| Lei et al. (2020) | $v$–$w$ | Single-layer | Explicit | Mohr–Coulomb | Cell-based strain averaging |
| Zhao and Choo (2020) | $u$–$p$ | Single-layer | Implicit | Elastic | Polynomial pressure projection |
| Cuomo et al. (2021) | $v$–$w$ | Single-layer | Explicit | Mohr–Coulomb | Nodal volumetric strain averaging |
| Kularathna et al. (2021) | $u$–$U$ | Single-layer | Semi-implicit | Mohr–Coulomb | Fractional time stepping |
| Zheng et al. (2021a) | $v$–$w$ | Single-layer | Explicit | Elastic | RI + MLSA patch recovery |
| Zheng et al. (2021b) | $u$–$p$–$U$ | Single-layer | Implicit | Elastic | RI + MLSA patch recovery |
| Martinelli and Galavi (2022) | $v$–$w$ | Single-layer | Explicit | Tresca & Modified Cam Clay | $\overline{\mathrm{B}}$ approach + Constant pore pressure in element |

respect to the solid being taken into account in the $v$–$w$ formulation (in essence, equivalent to the $u$–$U$ form described by Zienkiewicz et al. (1980), where $u$ and $U$ are the total displacements of the solid and fluid phases, respectively), while that is not the case for the simplified $u$–$p$ formulation. Although the $u$–$p$ formulation is known to be inaccurate for fast dynamic phenomena (Zienkiewicz et al., 1980), it has nevertheless served as a basis for a variety of coupled MPMs. In the context of coupled MPMs, both one and two sets of MPs have been adopted in the development of, respectively, single-layer and two-layer versions of the method — see Soga et al. (2015) for a discussion on their advantages and drawbacks. The lower computational costs that are normally associated with the single-layer approach have motivated its most frequent use in previous MPM research, as well as in this study. The time integration algorithm is another key factor in MPM modelling, as it can affect the overall stability and efficiency of the numerical scheme. As shown in Table 1, most coupled MPM formulations have so far been developed in combination with explicit, conditionally stable time integration. To allow the use of larger time steps and more convenient stability properties, semi-implicit (Kularathna et al., 2021) and fully implicit (Zhao and Choo, 2020; Zheng et al., 2021b) MPMs have recently begun to emerge in the literature.

Similarly to the case of coupled Finite Element Methods (FEMs), MPMs also perform poorly in the presence of incompressibility constraints when built on low-order spatial interpolation. With regard to fluid-saturated geomaterials, incompressible behaviour may be associated with hindered pore water drainage and/or a (nearly) isochoric response of the solid skeleton (Bandara and Soga, 2015). While the former may induce well-known instabilities in the simulated pore pressure field, the latter may give rise to an excessively stiff response of the system in hand (volumetric locking) – it is worth recalling that constitutive models for geomaterials produce only limited volumetric strain increments when substantial plasticity is mobilised. To suppress pore pressure instabilities in low-order coupled MPMs, several stabilisation approaches have been adopted, including fractional time stepping (Kularathna et al., 2021), polynomial pressure projection (Zhao and Choo, 2020), reduced integration (Abe et al., 2014; Bandara and Soga, 2015; Wang et al., 2018; Zheng et al., 2021a,b; Martinelli and Galavi, 2022), and volumetric strain averaging (Jassim et al., 2013; Ceccato et al., 2016; Lei et al., 2020). On the other hand, locking-related inaccuracies can be mitigated in two-phase coupled problems by means of techniques initially developed for one-phase media. In the context of one-phase MPM modelling, solutions based, e.g., on mixed variational principles (Mast et al., 2012; Iaconeta et al., 2019), fractional time stepping (Kularathna and Soga, 2017; Zhang et al., 2017), and $\overline{\mathrm{F}}$ and $\overline{\mathrm{B}}$ methods (Coombs et al., 2018; Bisht et al., 2021; Yuan et al., 2021), have already proven successful against locking in one-phase large-deformation problems. In very few instances, such locking remedies have also been implemented in coupled (standard) MPMs (Jassim et al., 2013; Bandara and Soga, 2015), but exclusively in combination with explicit time integration. Most recently, Kularathna et al. (2021) proposed a stable time-stepping scheme for the MPM modelling of fluid-saturated porous media within the framework of the Generalised Interpolation Material Point (GIMP) method (which is a variant of standard MPM).

This study demonstrates the benefits of combining the well-known anti-locking $\overline{\mathrm{B}}$ approach (originally proposed by Hughes (1980) for incompressible FEM modelling) with the fully implicit, three-field GIMP-patch method for two-phase poroelastic materials recently developed by Zheng et al. (2021b). The resulting method, named the 'implicit $\overline{\mathrm{B}}$ GIMP-patch' method, is shown to score two important goals: (i) it can substantially alleviate (undrained) pore pressure instabilities, owing to a beneficial combination of selective reduced integration and patch recovery based on a Moving Least Square Approximation (MLSA) (Zheng et al., 2021a); (ii) it exploits the $\overline{\mathrm{B}}$ approach to remedy locking-related inaccuracies in the presence of a (nearly) isochoric plastic behaviour of the solid skeleton.

To the authors' knowledge, the proposed combination of pressure stabilisation and anti-locking techniques is here explored for the first time in the framework of a fully implicit coupled MPM (within the framework of GIMP). The contents of the paper are organised as follows: after summarising in Section 2 the fundamentals of the earlier implicit GIMP-patch method (based on a $u$–$p$–$U$ formulation of the reference hydro-mechanical problem), technical details regarding the incorporation of the $\overline{\mathrm{B}}$ method are covered in Section 3; in Section 4 the performance of the proposed method is discussed with reference to a number of numerical verification examples.

## 2. Formulation of the implicit GIMP-patch method

In this section, the equations governing the dynamics of saturated soil-like materials based on the three-field $u$–$p$–$U$ formulation are first presented; then, the discretisation and stabilisation processes associated with the implicit GIMP-patch method are also summarised. Note that only those equations essential to a full understanding of the developments in this paper are presented. More details and further links to previous literature may be found in the recent work of Zheng et al. (2021b).

In what follows, a single set of MPs is used to represent both the soil skeleton and the pore fluid (water), with each material point storing information for both phases following the deformation of the solid

skeleton. The density of the soil–water mixture is obtained from the individual phase densities as $\rho = (1-n)\,\rho_s + n\rho_w$, where the subscripts $s$ and $w$ denote the solid and water phases, respectively, and $n$ is the volume porosity. Based on the well-established effective stress principle, the behaviour of the solid skeleton is assumed to be governed by the effective stress $\boldsymbol{\sigma}'$, defined, in vector notation, as $\boldsymbol{\sigma}' = \boldsymbol{\sigma} + \boldsymbol{m}p$, where $\boldsymbol{\sigma}$ is the total stress, $p$ the pore water pressure, and $\boldsymbol{m}$ the vector representation of the Kronecker tensor. In what follows, bold symbols indicate matrices and vectors, while positive values are used for tensile total/effective stress components and compressive pore pressures.

### 2.1. Governing equations

For fully-saturated porous media, the momentum balance equations associated with the whole two-phase mixture and the pore water phase read respectively as (Zienkiewicz and Shiomi, 1984; Zienkiewicz et al., 1999)

$$\mathbf{S}^{\mathrm{T}}\boldsymbol{\sigma} - \rho\ddot{\boldsymbol{u}} - \rho_w\ddot{\boldsymbol{u}}_r + \rho\boldsymbol{b} = \mathbf{0} \tag{1}$$

$$\nabla p - \boldsymbol{R} - \rho_w\ddot{\boldsymbol{u}} - \rho_w\frac{\ddot{\boldsymbol{u}}_r}{n} + \rho_w\boldsymbol{b} = \mathbf{0} \tag{2}$$

where $\mathbf{S}$ is a differential divergence operator, $\boldsymbol{u}$ is the absolute displacement of the soil skeleton, $\boldsymbol{u}_r$ is the displacement of the water phase relative to the solid phase and defined by $\boldsymbol{u}_r = n(\boldsymbol{U} - \boldsymbol{u})$ (where $\boldsymbol{U}$ is the absolute displacement of the water phase), $\boldsymbol{b}$ is an external body force, and $\boldsymbol{R}$ is the drag force exchanged by the soil skeleton and the pore water due to their relative motion; dots are used to indicate time differentiation.

The pore water flow must satisfy the following mass conservation equation:

$$\nabla\cdot\dot{\boldsymbol{u}}_r + \nabla\cdot\dot{\boldsymbol{u}} + \frac{\dot{p}}{Q} = \mathbf{0} \tag{3}$$

with the stiffness parameter $Q$ defined as $1/Q = n/K_w + (1-n)/K_s$, in which $K_w$ and $K_s$ are the bulk moduli of the water phase and soil particles, respectively.

In addition to the above conservation laws, hydraulic and mechanical constitutive relationships are also required, namely for the drag force $\boldsymbol{R}$ $\left(= \frac{n\rho_w g}{k}\left(\dot{\boldsymbol{U}} - \dot{\boldsymbol{u}}\right)\right)$, with $k$ and $g$ denoting the soil permeability and gravitational acceleration, respectively) and the soil skeleton behaviour. The latter is normally expressed by relating the rates of effective stress ($\dot{\boldsymbol{\sigma}}'$) and strain ($\dot{\boldsymbol{\varepsilon}}$):

$$\dot{\boldsymbol{\sigma}}' = \mathbf{D}^{ep}\dot{\boldsymbol{\varepsilon}} \tag{4}$$

where the elasto-plastic stiffness matrix of the solid skeleton ($\mathbf{D}^{ep}$) is used in combination with a linearised definition of the strain rate (Bardenhagen and Kober, 2004; Zhang et al., 2011; González Acosta et al., 2021; Tran and Sołowski, 2019; Zheng et al., 2021a; Lei et al., 2021a,b). It should be noted that this work focuses on the implementation of the $\overline{\mathrm{B}}$ approach in a coupled implicit MPM, and on its verification for coupled elastoplastic problems — particularly with respect to the notorious numerical oscillation issues that are often associated with MPM modelling (González Acosta et al., 2017, 2020; Zheng et al., 2021a). Fully general modelling of large deformations can be achieved by introducing well-established finite strain measures (Holzapfel, 2000) – such an extension is not expected to heavily impact the hydromechanical performance of the proposed method and will be pursued in future work.

### 2.2. Space and time discretisation

In the context of a three-field $u$–$p$–$U$ formulation, the primary variables $\boldsymbol{u}$ (solid displacement), $p$ (pore pressure) and $\boldsymbol{U}$ (fluid displacement) are first approximated using their nodal values ($\bar{\boldsymbol{u}}$, $\bar{\boldsymbol{p}}$ and $\bar{\boldsymbol{U}}$) in the background mesh:

$$\boldsymbol{u} = \mathbf{N}_u\bar{\boldsymbol{u}}, \qquad p = \boldsymbol{N}_p\bar{\boldsymbol{p}}, \qquad \boldsymbol{U} = \mathbf{N}_U\bar{\boldsymbol{U}} \tag{5}$$

where $\mathbf{N}_u$, $\boldsymbol{N}_p$ and $\mathbf{N}_U$ are matrices containing shape functions of the same low order (bilinear in 2D problems). Substituting the above approximations (Eq. (5)) into the weak form of the governing equations ((1), (2), and (3)) leads to the following discrete system of ordinary differential equations:

$$\begin{bmatrix} \mathbf{M}_u & \mathbf{0} & \mathbf{0} \\ \mathbf{0} & \mathbf{0} & \mathbf{0} \\ \mathbf{0} & \mathbf{0} & \mathbf{M}_U \end{bmatrix}\begin{bmatrix} \ddot{\bar{\boldsymbol{u}}} \\ \ddot{\bar{\boldsymbol{p}}} \\ \ddot{\bar{\boldsymbol{U}}} \end{bmatrix} + \begin{bmatrix} \mathbf{C}_1 & \mathbf{0} & -\mathbf{C}_2 \\ \mathbf{0} & \mathbf{0} & \mathbf{0} \\ -\mathbf{C}_2^{\mathrm{T}} & \mathbf{0} & \mathbf{C}_3 \end{bmatrix}\begin{bmatrix} \dot{\bar{\boldsymbol{u}}} \\ \dot{\bar{\boldsymbol{p}}} \\ \dot{\bar{\boldsymbol{U}}} \end{bmatrix} + \begin{bmatrix} \mathbf{K}_u & -\mathbf{G}_1 & \mathbf{0} \\ -\mathbf{G}_1^{\mathrm{T}} & \mathbf{P} & -\mathbf{G}_2^{\mathrm{T}} \\ \mathbf{0} & -\mathbf{G}_2 & \mathbf{0} \end{bmatrix}\begin{bmatrix} \bar{\boldsymbol{u}} \\ \bar{\boldsymbol{p}} \\ \bar{\boldsymbol{U}} \end{bmatrix} = \begin{bmatrix} \bar{\boldsymbol{f}}_s \\ \mathbf{0} \\ \bar{\boldsymbol{f}}_w \end{bmatrix} \tag{6}$$

where: $\mathbf{M}_u$ and $\mathbf{M}_U$ are mass matrices for the soil and water phases; $\mathbf{C}_1$, $\mathbf{C}_2$ and $\mathbf{C}_3$ are damping matrices physically associated with the grain–fluid drag (no Rayleigh damping included); $\mathbf{K}_u$ is the stiffness matrix of the solid skeleton; $\mathbf{P}$ is a compressibility matrix determined by the bulk stiffness of the solid grains and pore water; $\mathbf{G}_1$ and $\mathbf{G}_2$ are two matrices describing the hydro-mechanical coupling between the skeleton deformation and pore water flow; and $\bar{\boldsymbol{f}}_s$ and $\bar{\boldsymbol{f}}_w$ are nodal force vectors associated with the solid and water phases. The detailed expressions of these matrices emerge from the spatial discretisation process, and are provided by Zienkiewicz and Shiomi (1984) and Zheng et al. (2021b) with reference to FEM and MPM modelling, respectively.

Within the framework of MPM, the matrices in Eq. (6) can be obtained through the assembly of matrix contributions evaluated at the grid cell nodes after mapping from the MPs. If the same bilinear shape functions (in 2D problems) as in low-order FEM are used, then standard MPM results may suffer from spurious oscillations associated with discontinuous shape function gradients, particularly in the event of MP cell-crossing (Bardenhagen and Kober, 2004). To mitigate such oscillations, Bardenhagen and Kober (2004) proposed the GIMP approach, which is based on shape functions constructed by integrating linear shape functions $N_i(x)$ over the MP support domain $\Omega_{mp}$ – the subscripts $i$ and $mp$ indicate the $i$th node and $mp$th MP. For 1D problems, the GIMP shape function $S_i(x_{mp})$ (solid lines in Fig. 1(a)) and its gradient $B_i(x_{mp})$ (solid lines in Fig. 1(b)) are shown in Fig. 1, where $x_{mp}$ is the position of the $mp$th MP, and $2l_p$ defines the width of the support domain.

Using GIMP shape functions and their gradients, the matrices in the discrete system (6) can be re-obtained as shown in the Appendix. The whole equation set after space discretisation can be represented in the following compact form:

$$\mathbf{M}\boldsymbol{a} + \mathbf{C}\boldsymbol{v} + \mathbf{K}\boldsymbol{d} = \bar{\boldsymbol{f}} \tag{7}$$

where: $\mathbf{M}$, $\mathbf{C}$ and $\mathbf{K}$ are generalised mass, damping and stiffness matrices, respectively; $\bar{\boldsymbol{f}}$ is a time-varying external load term; $\boldsymbol{a} = \left[\ddot{\bar{\boldsymbol{u}}}, \ddot{\bar{\boldsymbol{p}}}, \ddot{\bar{\boldsymbol{U}}}\right]^{\mathrm{T}}$, $\mathbf{v} = [\dot{\bar{\boldsymbol{u}}}, \dot{\bar{\boldsymbol{p}}}, \dot{\bar{\boldsymbol{U}}}]^{\mathrm{T}}$, and $\boldsymbol{d} = [\bar{\boldsymbol{u}}, \bar{\boldsymbol{p}}, \bar{\boldsymbol{U}}]^{\mathrm{T}}$ are generalised nodal acceleration, velocity, and displacement vectors, respectively.

The ordinary differential system in Eq. (7) can be implicitly integrated in time using the well-established Newmark algorithm (Newmark, 1959). Using two time integration parameters, $\gamma$ and $\beta$, the corresponding recurrence relations for stepping from $n$ to $n+1$ are (Hughes, 1987):

$$\boldsymbol{a}_{n+1} = \boldsymbol{a}_n + \Delta\boldsymbol{a} \tag{8a}$$

$$\boldsymbol{v}_{n+1} = \boldsymbol{v}_n + \Delta t\left[(1-\gamma)\,\boldsymbol{a}_n + \gamma\boldsymbol{a}_{n+1}\right] \tag{8b}$$

$$\boldsymbol{d}_{n+1} = \boldsymbol{d}_n + \boldsymbol{v}_n\Delta t + \frac{\Delta t^2}{2}\left[(1-2\beta)\,\boldsymbol{a}_n + 2\beta\boldsymbol{a}_{n+1}\right] \tag{8c}$$

in which $\Delta t = t_{n+1} - t_n$ is the (constant) time step size. After substituting the above recurrence relations into Eq. (7), the following algebraic system of fully discretised equations is obtained:

$$\overline{\mathbf{K}}\Delta\boldsymbol{d}_{n+1} = \boldsymbol{f}_{n+1} - \boldsymbol{f}_n^{int} + \mathbf{M}_n\left[\frac{f_1}{\Delta t}\boldsymbol{v}_n + \left(\frac{f_1}{2} - 1\right)\boldsymbol{a}_n\right] + \mathbf{C}_n\left[\left(f_2 - 1\right)\boldsymbol{v}_n + \left(\frac{f_2}{2} - 1\right)\boldsymbol{a}_n\Delta t\right] \tag{9}$$

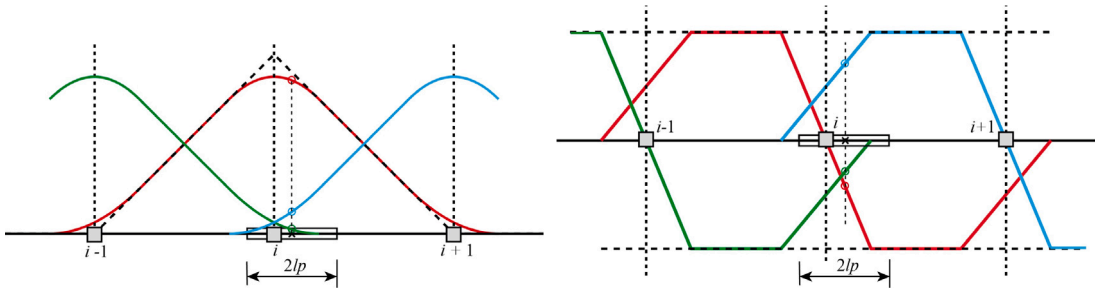


(a) GIMP shape function $S_i(x_{mp})$ (b) GIMP shape function gradient $B_i(x_{mp})$

**Fig. 1.** One-dimensional GIMP shape function and its gradient.

where $\overline{\mathbf{K}} = \frac{f_1}{\Delta t^2}\mathbf{M}_n + \frac{f_2}{\Delta t}\mathbf{C}_n + \mathbf{K}_n$ is an algorithmic dynamic stiffness matrix, based on the evaluations at the $n$th step of the generalised mass, damping and stiffness matrices ($\mathbf{M}_n$, $\mathbf{C}_n$ and $\mathbf{K}_n$, respectively); $f_1 = 1/\beta$, $f_2 = \gamma/\beta$, and $\boldsymbol{f}_n^{int} = \left[\boldsymbol{f}_{u,n}^{int}, \boldsymbol{f}_{p,n}^{int}, \boldsymbol{f}_{U,n}^{int}\right]^{\mathrm{T}}$ is the internal nodal force vector, in which

$$\boldsymbol{f}_{u,i}^{int} = \sum_{mp=1}^{N_{mp}} \mathbf{B}_{u,i}^{\mathrm{T}}\left(\boldsymbol{x}_{mp,n}\right)\left[\boldsymbol{\sigma}'_{mp,n} - (1-n)\,\boldsymbol{m}p_{mp,n}\right]V_{mp,n} \tag{10a}$$

$$f_{p,i}^{int} = \sum_{mp=1}^{N_{mp}}\left[-(1-n)\,S_{p,i}(\boldsymbol{x}_{mp,n})\varepsilon_{vol,mp}^{u} - S_{p,i}(\boldsymbol{x}_{mp,n})\frac{p_{mp,n}}{Q} - nS_{p,i}(\boldsymbol{x}_{mp,n})\varepsilon_{v,mp}^{U}\right]V_{mp,n} \tag{10b}$$

$$\boldsymbol{f}_{U,i}^{int} = -\sum_{mp=1}^{N_{mp}} \mathbf{B}_{U,i}^{\mathrm{T}}\left(\boldsymbol{x}_{mp,n}\right)n\boldsymbol{m}p_{mp,n}V_{mp,n} \tag{10c}$$

and $N_{mp}$ is the total number of MPs; $\varepsilon_{vol,mp}^{u}$ and $\varepsilon_{vol,mp}^{U}$ are the volumetric strain of the soil and water phases at the $mp$th MP; $\boldsymbol{x}_{mp,n}$ and $V_{mp,n}$ are the coordinate and volume of the $mp$th MP at step $n$, while $\boldsymbol{\sigma}'_{mp,n}$ and $p_{mp,n}$ indicate the corresponding effective stress and pore pressure values; and subscripts/superscripts $u$, $p$ and $U$, respectively, indicate variables associated with the primary variables in the $u$–$p$–$U$ formulation. In the remainder of this study, a single pair of integration parameters, $\beta = 0.25$ and $\gamma = 0.5$, is exclusively adopted.

Since elasto-plastic large-deformation problems are inevitably nonlinear, the discretised system (9) must be solved iteratively. To this end, each time step is solved through the Modified Newton–Raphson iteration scheme (Zienkiewicz et al., 2005). When equilibrium is reached, all relevant variables are updated at the MPs using the computed nodal values as follows:

$$\boldsymbol{a}_{mp,n+1}^{u} = \sum_{i=1}^{N_{node}} \mathbf{S}_{u,i}(\boldsymbol{x}_{mp,n})\ddot{\bar{\boldsymbol{u}}}_{i,n+1} \tag{11a}$$

$$\boldsymbol{a}_{mp,n+1}^{U} = \sum_{i=1}^{N_{node}} \mathbf{S}_{U,i}(\boldsymbol{x}_{mp,n})\ddot{\bar{\boldsymbol{U}}}_{i,n+1} \tag{11b}$$

$$\boldsymbol{v}_{mp,n+1}^{\alpha} = \boldsymbol{v}_{mp,n}^{\alpha} + \frac{\boldsymbol{a}_{mp,n+1}^{\alpha} + \boldsymbol{a}_{mp,n}^{\alpha}}{2}\Delta t \quad (\alpha = u, U) \tag{11c}$$

$$\boldsymbol{\sigma}'_{mp,n+1} = \boldsymbol{\sigma}'_{mp,n} + \mathbf{D}^{ep}\sum_{n=1}^{N_{node}} \mathbf{B}_{u,i}(\boldsymbol{x}_{mp,n})\bar{\boldsymbol{u}}_{i,n+1} \tag{11d}$$

$$p_{mp,n+1} = p_{mp,n} + \sum_{n=1}^{N_{node}} S_{p,i}(\boldsymbol{x}_{mp,n})\bar{p}_{i,n+1} \tag{11e}$$

$$\boldsymbol{x}_{mp,n+1} = \boldsymbol{x}_{mp,n} + \sum_{n=1}^{N_{node}} \mathbf{S}_{u,i}(\boldsymbol{x}_{mp,n})\bar{\boldsymbol{u}}_{i,n+1} \tag{11f}$$

where the superscripts $u$ and $U$ respectively denote variables associated with the solid and water phases, $N_{node}$ is the total number of nodes, $\ddot{\bar{\boldsymbol{u}}}_{i,n+1}$ is the solid acceleration for the $i$th node at the $(n+1)$th step (defined as $\frac{4\bar{\boldsymbol{u}}_{i,n+1}}{\Delta t^2} - \frac{4\dot{\bar{\boldsymbol{u}}}_{i,n}}{\Delta t} - \ddot{\bar{\boldsymbol{u}}}_{i,n}$[1]), $\ddot{\bar{\boldsymbol{U}}}_{i,n+1}$ is the water nodal acceleration (calculated as $\frac{4\bar{\boldsymbol{U}}_{i,n+1}}{\Delta t^2} - \frac{4\dot{\bar{\boldsymbol{U}}}_{i,n}}{\Delta t} - \ddot{\bar{\boldsymbol{U}}}_{i,n}$), and $\bar{\boldsymbol{u}}_{i,n+1}$ and $\bar{p}_{i,n+1}$ are the nodal incremental displacement of the solid phase and the nodal incremental pore pressure. Since this study considers a single-layer MPM formulation, the positions of the MPs are updated following the motion of the solid phase.

To alleviate pore pressure instabilities in coupled analyses, a patch recovery algorithm based on a Moving Least Square Approximation (MLSA) has been introduced in the implicit GIMP method by Zheng et al. (2021b) after an earlier explicit implementation (Zheng et al., 2021a). In the MLSA-based patch recovery, a rectangular area can be delimited around a node using central GPs in the four neighbouring quadrilateral grid cells; therefore, a linear patch can be defined within this area using the mapped pore pressure increments at central GPs. The pore pressure increments at MPs are thus determined by the established MLSA-based linear patch. More details regarding the fundamentals of the reference patch recovery algorithm can be found in Zienkiewicz and Zhu (1992) and Zheng et al. (2021a). The implicit GIMP-patch method was first tested for poroelastic coupled problems by Zheng et al. (2021b) and proven to produce stable and oscillation-free solutions. As the implicit GIMP method is not covered further herein, interested readers are referred to Zheng et al. (2021b).

## 3. Implementation of the $\overline{\mathbf{B}}$ locking antidote into the implicit GIMP-patch method

In a similar manner to low-order FEMs, the accuracy of the coupled implicit GIMP-patch method may also be negatively impacted by volumetric locking effects, which are likely to manifest themselves when the soil skeleton deforms at (nearly) constant volume (e.g., during plastic flow) and a full strain integration is adopted in the stress analysis (Coombs et al., 2018). In this study, the original version of the $\overline{\mathbf{B}}$ method for low-order FEMs (Hughes, 1980) is implemented in the implicit GIMP-patch method to remedy locking-related inaccuracies in elasto-plastic large-deformation problems. The essence of the $\overline{\mathbf{B}}$ approach is to evaluate the excessively stiff volumetric component of the compatibility matrix ($\mathbf{B}_i$) via reduced quadrature, while full quadrature is still employed for the complementary deviatoric part (Hughes, 1980). Accordingly, the compatibility matrix $\mathbf{B}_i$ is first split at a given node $i$ into deviatoric ($\mathbf{B}_i^{dev}$) and volumetric ($\mathbf{B}_i^{vol}$) components, so that $\mathbf{B}_i = \mathbf{B}_i^{dev} + \mathbf{B}_i^{vol}$. In the case of plane strain conditions, the $\mathbf{B}_i$ and $\mathbf{B}_i^{vol}$

[1] The recurrence relation for the solid acceleration at step $n+1$ is obtained by substituting Eq. (8c) into Eq. (8a). More details can be found in Hughes (1987) and Zheng et al. (2021b).

matrices assume the following forms:

$$\mathbf{B}_i = \begin{bmatrix} \frac{\partial N_i}{\partial x} & 0 \\ 0 & \frac{\partial N_i}{\partial y} \\ \frac{\partial N_i}{\partial y} & \frac{\partial N_i}{\partial x} \\ 0 & 0 \end{bmatrix}, \qquad \mathbf{B}_i^{vol} = \frac{1}{3}\begin{bmatrix} \frac{\partial N_i}{\partial x} & \frac{\partial N_i}{\partial y} \\ \frac{\partial N_i}{\partial x} & \frac{\partial N_i}{\partial y} \\ 0 & 0 \\ \frac{\partial N_i}{\partial x} & \frac{\partial N_i}{\partial y} \end{bmatrix}, \qquad \mathbf{B}_i^{dev} = \mathbf{B}_i - \mathbf{B}_i^{vol} \tag{12}$$

where $N_i$ is the shape function associated with the $i$th node.

In the FEM $\overline{\text{B}}$ method, the original volumetric matrix $\mathbf{B}_i^{vol}$ is replaced by the following 'improved' version evaluated at the grid cell centres (gc):

$$\overline{\mathbf{B}}_i^{vol} = \frac{1}{3}\begin{bmatrix} \frac{\partial N_{i,gc}}{\partial x} & \frac{\partial N_{i,gc}}{\partial y} \\ \frac{\partial N_{i,gc}}{\partial x} & \frac{\partial N_{i,gc}}{\partial y} \\ 0 & 0 \\ \frac{\partial N_{i,gc}}{\partial x} & \frac{\partial N_{i,gc}}{\partial y} \end{bmatrix} \tag{13}$$

while the deviatoric matrix $\mathbf{B}_i^{dev}$ is directly calculated at the Gauss point (gp) locations. As a result, the following global compatibility matrix $\overline{\mathbf{B}}_i$ is obtained:

$$\overline{\mathbf{B}}_i = \mathbf{B}_i^{dev} + \overline{\mathbf{B}}_i^{vol} = \begin{bmatrix} \frac{2}{3}\frac{\partial N_{i,gp}}{\partial x} + \frac{1}{3}\frac{\partial N_{i,gc}}{\partial x} & -\frac{1}{3}\frac{\partial N_{i,gp}}{\partial y} + \frac{1}{3}\frac{\partial N_{i,gc}}{\partial y} \\ -\frac{1}{3}\frac{\partial N_{i,gp}}{\partial x} + \frac{1}{3}\frac{\partial N_{i,gc}}{\partial x} & \frac{2}{3}\frac{\partial N_{i,gp}}{\partial y} + \frac{1}{3}\frac{\partial N_{i,gc}}{\partial y} \\ \frac{\partial N_{i,gp}}{\partial y} & \frac{\partial N_{i,gp}}{\partial x} \\ -\frac{1}{3}\frac{\partial N_{i,gp}}{\partial x} + \frac{1}{3}\frac{\partial N_{i,gc}}{\partial x} & -\frac{1}{3}\frac{\partial N_{i,gp}}{\partial y} + \frac{1}{3}\frac{\partial N_{i,gc}}{\partial y} \end{bmatrix} \tag{14}$$

The same $\overline{\text{B}}$ approach has been previously incorporated into two-phase standard MPM (Bandara and Soga, 2015; Martinelli and Galavi, 2022) and one-phase GIMP (Bisht et al., 2021; Yuan et al., 2021), in both cases within an explicit time stepping scheme. It should be noted that such an implementation can easily be performed for a standard MPM, since the centre of each grid cell can be directly determined. In contrast, the $\overline{\text{B}}$ extension of GIMP is less straightforward – a specific MP may in fact be influenced by multiple cells when its support domain lies across more than one grid cell, which frequently happens during the movement of MPs. Following the approach proposed by Coombs et al. (2018), only that portion of the MP support domain lying within the domain of a grid cell is considered to contribute to the volumetric behaviour of the cell itself.

In order to construct the GIMP shape function and its gradient, the shape function $N_{i,gc}$ and its gradient $\nabla N_{i,gc}$ take values at the centre of a grid cell, which remain constant ($N_{i,gc} = \frac{1}{2}$ and $\nabla N_{i,gc} = \pm\frac{1}{h}$, where $h$ is the size of a quadrilateral cell in a regular background mesh) through the entire cell. The one-dimensional GIMP shape function $S_{i,gc}$ is then computed as

$$S_{i,gc} = \frac{1}{V_{mp}}\int_{\Omega_{mp}} \frac{1}{2}\mathrm{d}x \tag{15}$$

Fig. 2 shows the GIMP shape functions and their gradients sampled at the centre of the grid cell. Using the GIMP shape function, the modified $\bar{\mathbf{B}}_i$ matrix can be written as

$$\bar{\mathbf{B}}_i = \begin{bmatrix} \frac{2}{3}\frac{\partial S_{i,mp}}{\partial x} + \frac{1}{3}\frac{\partial S_{i,gc}}{\partial x} & -\frac{1}{3}\frac{\partial S_{i,mp}}{\partial y} + \frac{1}{3}\frac{\partial S_{i,gc}}{\partial y} \\ -\frac{1}{3}\frac{\partial S_{i,mp}}{\partial x} + \frac{1}{3}\frac{\partial S_{i,gc}}{\partial x} & \frac{2}{3}\frac{\partial S_{i,mp}}{\partial y} + \frac{1}{3}\frac{\partial S_{i,gc}}{\partial y} \\ \frac{\partial S_{i,mp}}{\partial y} & \frac{\partial S_{i,mp}}{\partial x} \\ -\frac{1}{3}\frac{\partial S_{i,mp}}{\partial x} + \frac{1}{3}\frac{\partial S_{i,gc}}{\partial x} & -\frac{1}{3}\frac{\partial S_{i,mp}}{\partial y} + \frac{1}{3}\frac{\partial S_{i,gc}}{\partial y} \end{bmatrix} \tag{16}$$

After determining the modified $\bar{\mathbf{B}}_i$ matrix, the nodal stiffness and internal force matrices (see the Appendix for more details) in Eq. (9) and the effective stress vector in Eq. (11d) can be computed by simply replacing the original $\mathbf{B}$ matrix with the modified $\bar{\mathbf{B}}_i$ matrix. Aside from the inclusion of the $\bar{\mathbf{B}}$ matrix, all other steps regarding space and time discretisation are the same as in the implicit GIMP-patch method proposed by Zheng et al. (2021b).

**Table 2**
Material properties adopted for the footing and the (two-phase) soil for the total stress analysis of the undrained bearing capacity problem in Fig. 3.

| Property | Symbol | Unit | SD analysis | LD analysis |
|---|---|---|---|---|
| Young's modulus (footing) | $E_f$ | [kPa] | 10000 | 10000 |
| Poisson's ratio (footing) | $\nu_f$ | [–] | 0.3 | 0.3 |
| Young's modulus | $E$ | [kPa] | 1000 | 100 |
| Poisson's ratio | $\nu$ | [–] | 0.49 | 0.49 |
| Soil grain density | $\rho_s$ | [kg/m$^3$] | 2600 | 2600 |
| Water density | $\rho_w$ | [kg/m$^3$] | 1000 | 1000 |
| Friction angle | $\phi$ | [°] | 0 | 0 |
| Dilation angle | $\psi$ | [°] | 0 | 0 |
| Cohesion | $c$ | [kPa] | 0.1 | 1.0 |
| Initial porosity | $n$ | [–] | 0.4 | 0.4 |
| Water bulk modulus | $K_w$ | [kPa] | $2.2\times10^6$ | $2.2\times10^6$ |
| Soil grain bulk modulus | $K_s$ | [kPa] | $1.0\times10^{10}$ | $1.0\times10^{10}$ |
| Permeability | $k$ | [m/s] | $1.0\times10^{-1}$ | $1.0\times10^{-1}$ |

## 4. Numerical verification and application examples

This section presents the numerical solutions obtained for several verification and application examples using the proposed implicit $\overline{\text{B}}$ GIMP-patch method. In all examples, the mechanical behaviour of the soil skeleton is reproduced by the Mohr–Coulomb model, based on a model implementation that does not include a tension cut-off (not a point of focus in this study).

### 4.1. Bearing capacity of a strip footing

Numerical studies regarding the undrained bearing capacity of rough strip footings have often been performed by modelling the soil as a single-phase incompressible material (total stress analysis), both under small- and large-deformation conditions. Such a reference problem has recently been studied by Kiriyama and Higo (2020) and Bisht et al. (2021) via single-phase MPM simulations. As a preliminary verification of the implicit $\overline{\text{B}}$ GIMP-patch method, its single-phase, total stress performance is first verified with respect to the bearing capacity problem shown in Fig. 3 (the symmetry with respect to the median plane has been exploited to reduce the computational cost). To comply with the total stress approach, the inherently two-phase numerical model has been set up to function as a one-phase system by (i) introducing a very large permeability, and (ii) reducing the Mohr–Coulomb frictional model to its cohesive/isochoric version (Tresca model, in which the cohesion $c$ coincides with the undrained strength $s_u$) – all material properties are listed in Table 2. As is usual in total stress limit load calculations, the initial stress state of the soil is not influential and, therefore, there is no need to account for its self-weight in the analysis (although a mass density is still assigned to the MPs for the calculation of the inertial terms associated with the $u$–$p$–$U$ formulation).

Both the footing (breadth $B = 1$ m) and the soil layer have been discretised using 4-node quadrilateral grid cells, with each cell initially hosting $2 \times 2$ equally-spaced MPs. To enable meaningful comparison to static, one-phase solutions, the external load has been applied at a sufficiently slow rate, so as to ensure negligible acceleration and excess pore pressure generation. Both numerical simulations have been performed with a time step size equal to $\Delta t = 5.0\times10^{-2}$ s, and by adopting the same material parameters as those adopted by Bisht et al. (2021) for fair comparison. The selected time step size and loading rate have been verified to enable proper modelling of the inherently quasi-static process under consideration using the fully dynamic MPM formulation developed in this study.

#### 4.1.1. Small-deformation analysis

The small-deformation (SD) analysis of the problem in Fig. 3 has been performed in combination with a large ratio between the Young's modulus and the cohesion (undrained shear strength) of the soil, $E/c = 10000$, so as to achieve the bearing capacity limit – $q/c = 2 + \pi \approx 5.14$

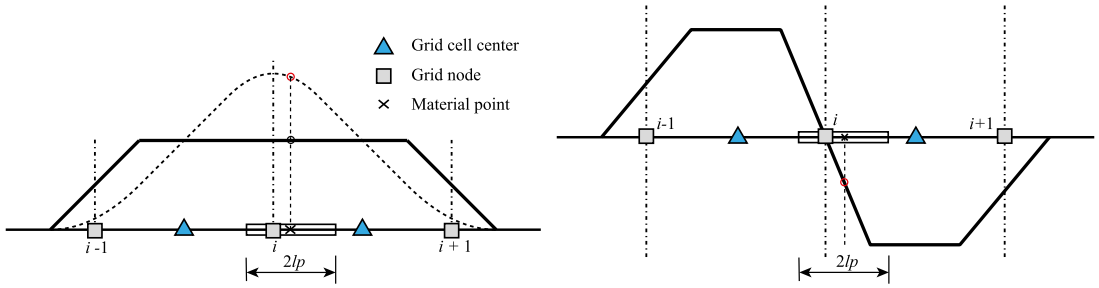


(a) GIMP shape function (b) GIMP shape function gradient

**Fig. 2.** One-dimensional GIMP shape function and its gradient sampled at the centre of a grid cell.

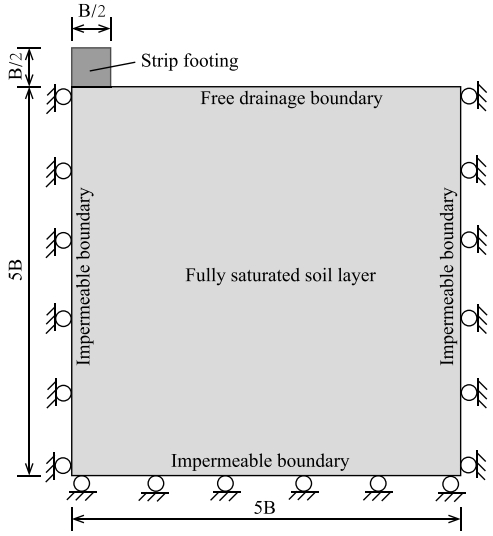


**Fig. 3.** Reference bearing capacity problem for a strip footing: computational domain and boundary conditions.

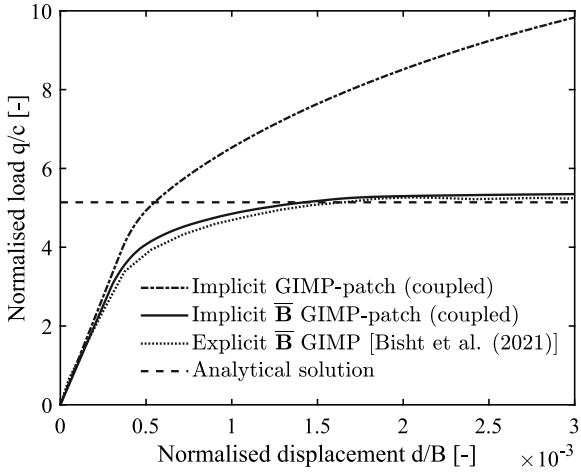


**Fig. 4.** SD relationship between normalised load ($q/c$) and displacement ($d/B$) for the undrained bearing capacity problem in Fig. 3.

– with only a small settlement of the foundation. In this SD example the external vertical pressure $q$ has been directly applied on the grid nodes below the footing, at a rate of 0.01 kPa/s. Fig. 4 shows the SD relationship between the normalised load ($q/c$) and displacement ($d/B$) obtained for a grid cell size $h$ equal to 0.25 m. In Fig. 4, the implicit $\overline{\text{B}}$ GIMP-patch solution is compared to those solutions obtained via the previous implicit GIMP-patch method by Zheng et al. (2021b) and the explicit $\overline{\text{B}}$ GIMP by Bisht et al. (2021). It is apparent that the implicit GIMP-patch solution severely overestimates the analytical capacity limit, while excellent agreement is observed between the result obtained by the method proposed in this study and the result obtained by Bisht et al. (2021). This outcome supports the anti-locking effectiveness of the implicit $\overline{\text{B}}$ GIMP-patch method, with a computational convenience that is expected to be superior to Bisht et al.'s method owing to the implicit time stepping scheme.

In more detail, Fig. 5 displays the final distributions of the mean stress obtained through the implicit GIMP-patch method, as computed using both its original and $\overline{\text{B}}$ versions. Even for an SD analysis in which the displacements are negligible, Fig. 5(a) shows that the implicit GIMP-patch method generates spurious stress oscillations when no anti-locking measures are undertaken. In contrast, the corresponding picture arising from the $\overline{\text{B}}$ analysis shows the typical compression bulb under the foundation without any undesired oscillations (Fig. 5(b)).

To explore the influence of space discretisation in the implicit $\overline{\text{B}}$ GIMP-patch method, Fig. 6 shows the load–displacement curves obtained with four different space discretisations ($h$ = 0.5 m, 0.25 m, 0.1 m, and 0.05 m). In all cases, the implicit $\overline{\text{B}}$ GIMP-patch solution captures the undrained bearing capacity of the strip footing, with a clearly converging trend towards Prandtl's solution as finer background meshes are considered.

#### 4.1.2. *Large-deformation analysis*

The static, undrained bearing capacity of a strip footing under large deformations (LD) has previously been studied within a one-phase total stress framework using a variety of numerical methods, including the Arbitrary Lagrangian–Eulerian (ALE) approach (Nazem et al., 2006, 2009), sequential limit analysis (Da Silva et al., 2011), the remeshing and interpolation technique with small strain (RITSS) (Wang et al., 2015), and MPM (Sołowski and Sloan, 2015; Woo and Salgado, 2018; Iaconeta et al., 2019; Kiriyama and Higo, 2020; Bisht et al., 2021). In what follows, the LD performance of the (coupled) implicit $\overline{\text{B}}$ GIMP-patch method is assessed, following the same adopted strategy as in the previous SD sub-section, i.e., with a sufficiently slow application of the external load (0.1 kPa/s) and, therefore, negligible pore pressure build-up. It is also worth mentioning that, within the MPM framework, it is rather difficult to exactly enforce natural boundary conditions such as surface tractions, due to the substantial displacement of MPs associated with LD processes. Therefore, it has been preferred to model the footing in Fig. 3 as a solid of increasing unit weight, which easily enables the application of a desired vertical pressure — as previously done by Kiriyama and Higo (2020). For comparison purposes, the simulated load–displacement curve for the foundation has been obtained by calculating the external pressure via the average contact force between the footing block and the underlying (weightless) soil.

In Fig. 7, the load–displacement curves obtained through the implicit $\overline{\text{B}}$ GIMP-patch method, and grid cell sizes of $h$ = 0.25 m and

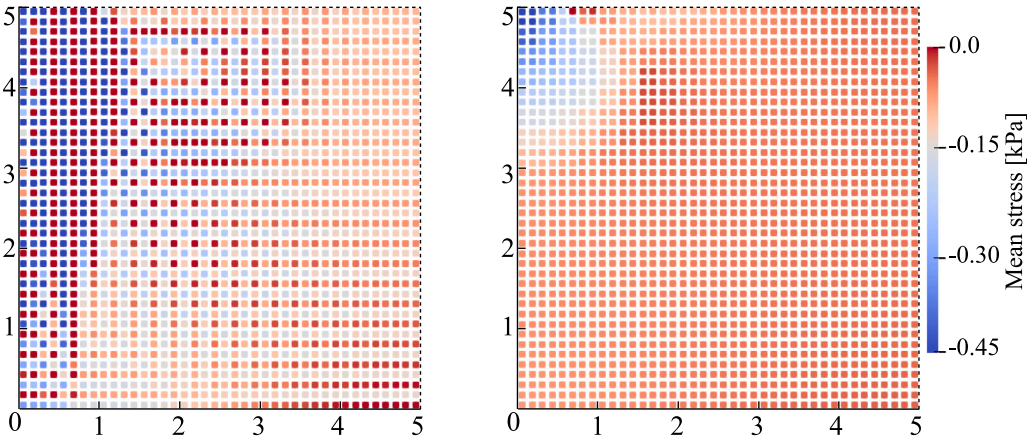


(a) implicit GIMP-patch method (b) implicit $\overline{\text{B}}$ GIMP-patch method

**Fig. 5.** SD mean stress distribution associated with the last calculation step of the analyses in Fig. 4: (a) implicit GIMP-patch method by Zheng et al. (2021b) vs (b) implicit $\overline{\text{B}}$ GIMP-patch method (this study). The horizontal and vertical axes refer to distance non-dimensionalised with respect to the foundation width $B$.

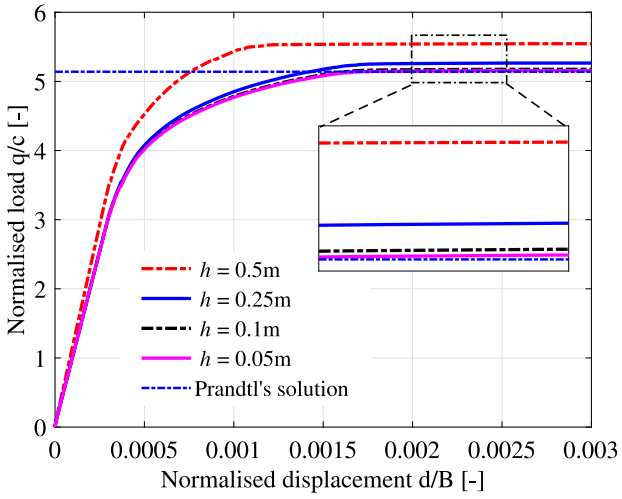


**Fig. 6.** SD mesh sensitivity of the implicit $\overline{\text{B}}$ GIMP-patch method for the undrained bearing capacity problem in Fig. 3 (including a zoom-in on the detail at bearing failure).

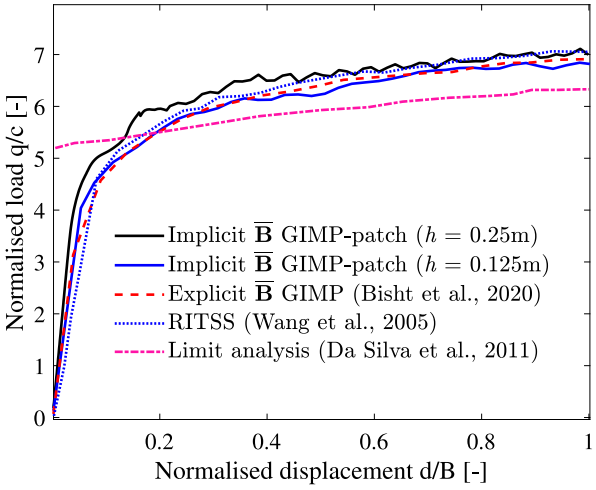


**Fig. 7.** LD normalised load–displacement curves for the undrained bearing capacity problem in Fig. 3.

0.125 m, are plotted. The LD solutions from explicit $\overline{\text{B}}$ GIMP (Bisht et al., 2021), RITSS (Wang et al., 2015), and sequential limit analysis (Da Silva et al., 2011) are also included for comparison — note that the soil is modelled as a strictly rigid-plastic material in the case of sequential limit analysis (Da Silva et al., 2011), whereas typical elasto-plastic behaviour is assumed in all other numerical solutions. It can be observed that the implicit $\overline{\text{B}}$ GIMP-patch solution is in good agreement with other LD results from the literature. The small differences between the $\overline{\text{B}}$ GIMP-patch solutions and the other solutions are likely to be due to the use of a relatively coarse/structured grid in this study, while locally refined meshes have been adopted in the referenced studies.

To further assess the LD performance of the implicit $\overline{\text{B}}$ GIMP-patch method, Fig. 8 illustrates the distributions of the mean (effective) stress distribution and the deviatoric plastic strain invariant $\epsilon_p^d = \sqrt{2/3}\boldsymbol{e}_p : \boldsymbol{e}_p$ (with $\boldsymbol{e}_p$ being the deviatoric plastic strain tensor) associated with a normalised settlement of the footing equal to $d/B = 1$. Also under LD conditions, the mean stress field is mostly oscillation-free and exhibits a well-shaped compression bulb — see Fig. 8(a); in Fig. 8(b), large values of deviatoric plastic strain appear around the foundation, which compare well with the quantitative observations of Iaconeta et al. (2019) and Bisht et al. (2021). However, some small oscillations are still visible near the bottom-right corner of the footing block, where substantial relocation of the MPs takes place during the large settlement of the foundation. Such a relocation can lead to a discontinuous support domain of MPs (see also Charlton, 2018) and, as a consequence, cause stress oscillations (though not due to locking effects). Furthermore, positive (tensile) values of the mean effective stress can be observed around the bottom-right corner of the footing, in a fashion similar to the results shown by Bisht et al. (2021). Combining a constitutive tension cut-off with a more advanced algorithm for support-domain updating – of the kind proposed in previous studies (Sadeghirad et al., 2011; Charlton, 2018; Coombs et al., 2020) – is expected to positively impact stress recovery calculations.

### 4.2. Earthen slope failure

In this section, the performance of the implicit $\overline{\text{B}}$ GIMP-patch method is evaluated with respect to slope failure processes triggered by gravity. As is shown in Fig. 9, the reference slope comprises two soil layers that are henceforth referred to as 'upper' and 'lower' (foundation) layers — all material properties are listed in Table 3. The free surface of the slope is unconstrained and freely draining, while the lateral and bottom boundaries are impermeable and supported by rollers. In both example cases considered hereafter, the problem domain has

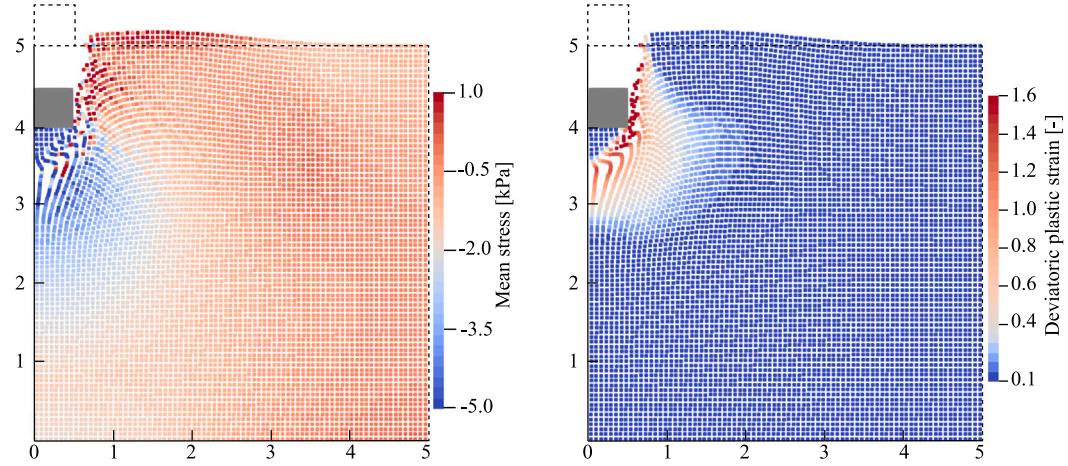


**Fig. 8.** LD mean stress and deviatoric plastic strain distributions associated with the last calculation step of the analyses in Fig. 7 (grid cell size $h = 0.125$ m). The horizontal and vertical axes refer to distance non-dimensionalised with respect to the foundation width $B$.

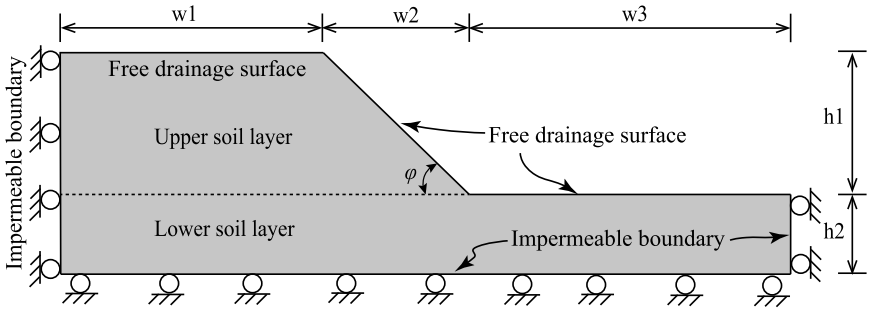


**Fig. 9.** Reference slope stability problem: computational domain and boundary conditions.

**Table 3**
Soil properties associated with the reference slope in Fig. 9.

| Property | Symbol | Clay slope | | Sand slope | |
|---|---|---|---|---|---|
| | | Upper layer | Lower layer | Upper layer | Lower layer |
| Young's modulus | $E$ [kPa] | 1000 | 1000 | 1000 | 1000 |
| Poisson's ratio | $\nu$ [–] | 0.49 | 0.49 | 0.3 | 0.3 |
| Soil grain density | $\rho_s$ [kg/m$^3$] | 2650 | 2650 | 2650 | 2650 |
| Water density | $\rho_w$ [kg/m$^3$] | 1000 | 1000 | 1000 | 1000 |
| Friction angle | $\phi$ [°] | 0 | 0 | 25 | 25 |
| Initial dilation angle | $\psi_{ini}$ [°] | 0 | 0 | −5 | −5 |
| Critical dilation angle | $\psi_r$ [°] | 0 | 0 | 0 | 0 |
| Dilation evolution parameter | $\eta$ [–] | – | – | −25.0 | −25.0 |
| Peak cohesion | $c_p$ [kPa] | 6.4 | 20.0 | 3.0 | 20.0 |
| Residual cohesion | $c_r$ [kPa] | 3.6 | 20.0 | 3.0 | 20.0 |
| Deviatoric plastic strain for $c_r$ | $\epsilon_p^r$ [–] | 0.75 | 0.75 | – | – |
| Initial porosity | $n$ [–] | 0.4 | 0.4 | 0.4 | 0.4 |
| Water bulk modulus | $K_w$ [kPa] | $2.2 \times 10^6$ | $2.2 \times 10^6$ | $2.2 \times 10^6$ | $2.2 \times 10^6$ |
| Soil grain bulk modulus | $K_s$ [kPa] | $1.0 \times 10^{10}$ | $1.0 \times 10^{10}$ | $1.0 \times 10^{10}$ | $1.0 \times 10^{10}$ |
| Permeability | $k$ [m/s] | $1.0 \times 10^{-1}$ | $1.0 \times 10^{-1}$ | $1.0 \times 10^{-1} \sim 1.0 \times 10^{-6}$ | |

been discretised by means of four-node quadrilateral grid cells of size 0.2 m × 0.2 m, with each cell initially hosting four equally-spaced MPs; implicit time integration has been performed with a time step size of $\Delta t = 5.0 \times 10^{-2}$ s.

#### 4.2.1. Undrained analysis of slope failure in softening clay

Undrained slope failure is simulated by resorting to the same total stress approach adopted in Section 4.1 — a Tresca-like soil behaviour has been introduced to obtain an isochoric material response. To reproduce the gradual reduction in undrained strength during soil sliding, a simple cohesion degradation mechanism has been incorporated into the constitutive law (Wang et al., 2018); specifically, by prescribing a linear reduction between the peak ($c_p$) and residual ($c_r$) shear strength values with accumulated plastic deviatoric strain $\epsilon_p^d$, and $c_r$ being attained for a value of $\epsilon_p^d$ equal to $\epsilon_p^r$, with the latter being an additional material parameter. Note that a much larger strength is assigned to the foundation layer (Table 3), in order to force slope failure to occur within the upper layer. Furthermore, the investigation of possible grid-dependence effects associated with strain-softening are out of the scope of this study. The size of the computational domain is defined, with reference to Fig. 9, by $w_1 = 4.0$ m, $w_2 = 2.0$ m, $w_3 = 4.0$ m, $h_1 = 2.0$ m, and $h_2 = 1.0$ m, with the slope inclination being $\varphi = 45°$.

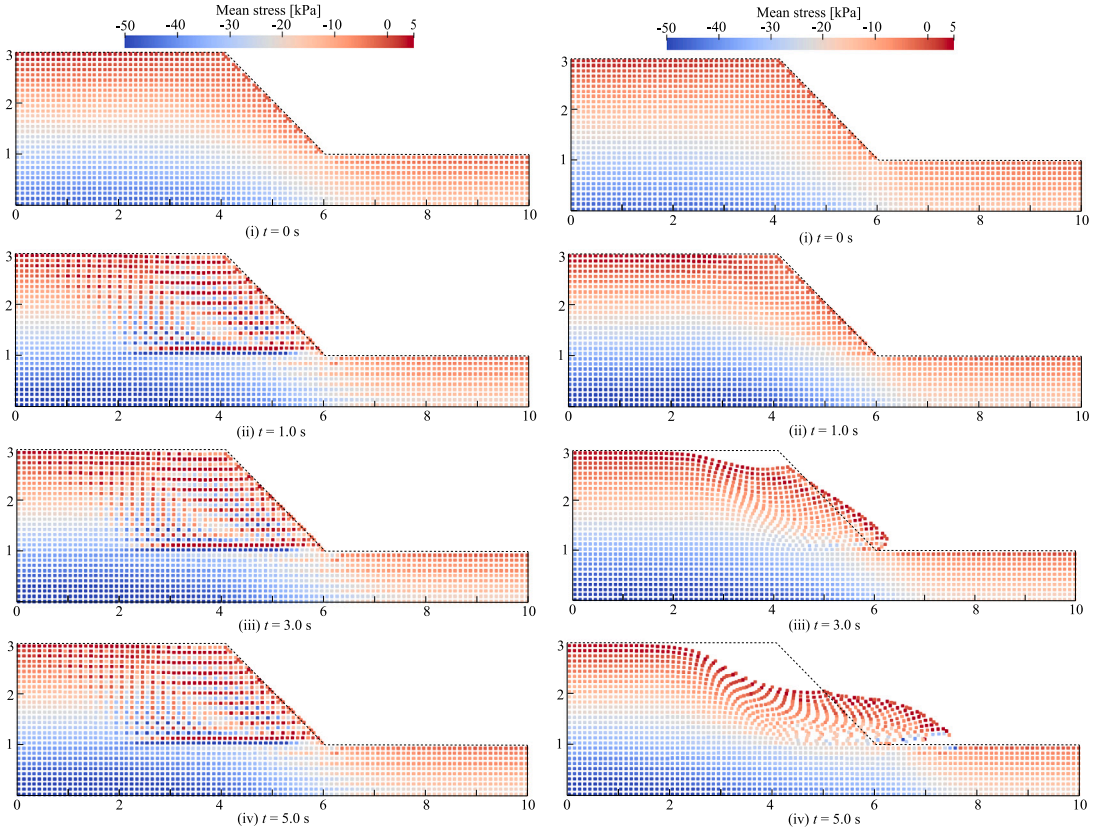


**Fig. 10.** Time evolution of mean stress in the soil during undrained slope failure in softening clay. Results obtained through (a) implicit GIMP-patch method and (b) implicit $\overline{\mathrm{B}}$ GIMP-patch method.

Two slope failure analyses have been carried out using both the original and $\overline{\mathrm{B}}$ versions of the implicit GIMP-patch method, according to the following two steps: (i) generation of the initial soil stresses by gradually applying gravity in combination with kinematic constraints to prevent immediate slope deformation; (ii) free slope deformation and failure under its own weight with a degrading cohesion (the peak cohesion in Table 3 has been purposely selected to render the 45° slope unstable). In contrast to the footing problem in Section 4.1, the gravity-driven failure of a slope does not allow the attainment of a limit response with exactly no pore pressure build-up, not even if a very large permeability value is used. Therefore, the pore pressure degrees-of-freedom have been forcedly set to zero in the MPM code to study the anti-locking performance of the implicit $\overline{\mathrm{B}}$ GIMP strategy in a large-deformation problem involving material plasticity and softening.

Fig. 10 shows the mean (total) stress contours at four different time instants, namely $t = 0$ s, 1.0 s, 3.0 s, and 5.0 s. Fig. 10(a) confirms that severe stress oscillations are returned by the implicit GIMP-patch method without a proper mitigation of volumetric locking. Such oscillations become particularly apparent where plastic straining takes place most intensely (i.e., near the interface between upper and lower layers — see Fig. 11), and tend to become more severe over time. In contrast, the benefits of the $\overline{\mathrm{B}}$ technique are confirmed once again in Fig. 10(b), even in the presence of material softening. Furthermore, Fig. 11 also shows how locking can significantly affect the slope failure mechanism: the implicit GIMP-patch method returns a completely 'locked' deformation pattern, whereas significant slope run-out is obtained with the $\overline{\mathrm{B}}$-enhanced calculations. This confirms the possibly extreme consequences of volumetric locking, and the practical importance of its remediation in large-deformation problems.

#### 4.2.2. Coupled analysis of slope failure in water-saturated sand

In this example, the coupled analysis of a sandy slope collapsing under its self-weight is tackled using the implicit $\overline{\mathrm{B}}$ GIMP-patch method. The problem domain in Fig. 9 is defined by $w_1 = 4.0$ m, $w_2 = 2.0$ m, $w_3 = 5.0$ m, $h_1 = 2.0$ m, and $h_2 = 1.0$ m, and the slope inclination is $\varphi = 45°$.

Sand behaviour has been simply modelled through the standard, state-independent Mohr–Coulomb model. To more realistically capture the contractive plastic response of a loose sand, a negative initial dilation angle ($\psi_{ini}$) has been adopted at the beginning of the analysis; upon plastic straining, the dilation angle evolves with deviatoric plastic strain $\epsilon_p^d$ towards its (nil) critical state value ($\psi_{crit}$) according to the following relationship (Lei et al., 2020):

$$\psi = \psi_{crit} + \left(\psi_{ini} - \psi_{crit}\right) e^{-\eta \epsilon_p^d} \tag{17}$$

where $\eta$ is a material parameter governing the variation of $\psi$ with $\epsilon_p^d$. The material properties chosen for this example are listed in Table 3 and include, for simplicity, constant values of cohesion and frictional angle. Some small cohesion has been introduced for the upper layer to enable smoother calculations under low mean effective stress; conversely, an unrealistically large cohesion has been set for the foundation layer, with the sole goal of containing the slope failure within the upper layer.

Fig. 12 shows the contours of pore pressure and mean effective stress at four different time instants, obtained with a soil permeability $k$ of $1.0 \times 10^{-4}$ m/s. The gradual development of slope failure due to shear banding is also visible and the slope face (indicated by the dashed line) is compared to the initial geometry (indicated by the dotted line). During all phases of the slope failure, the implicit $\overline{\mathrm{B}}$ GIMP-patch method returns perfectly smooth, oscillation-free distributions of effective stress

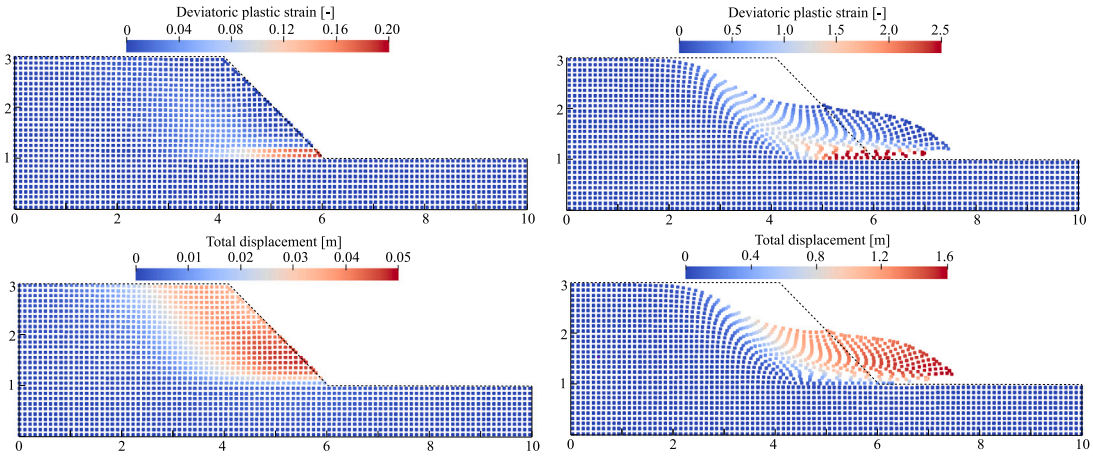


**Fig. 11.** Final distributions of deviatoric plastic strain and total displacement associated with undrained slope failure in softening clay. Results obtained through (a) implicit GIMP-patch method and (b) implicit $\overline{B}$ GIMP-patch method.

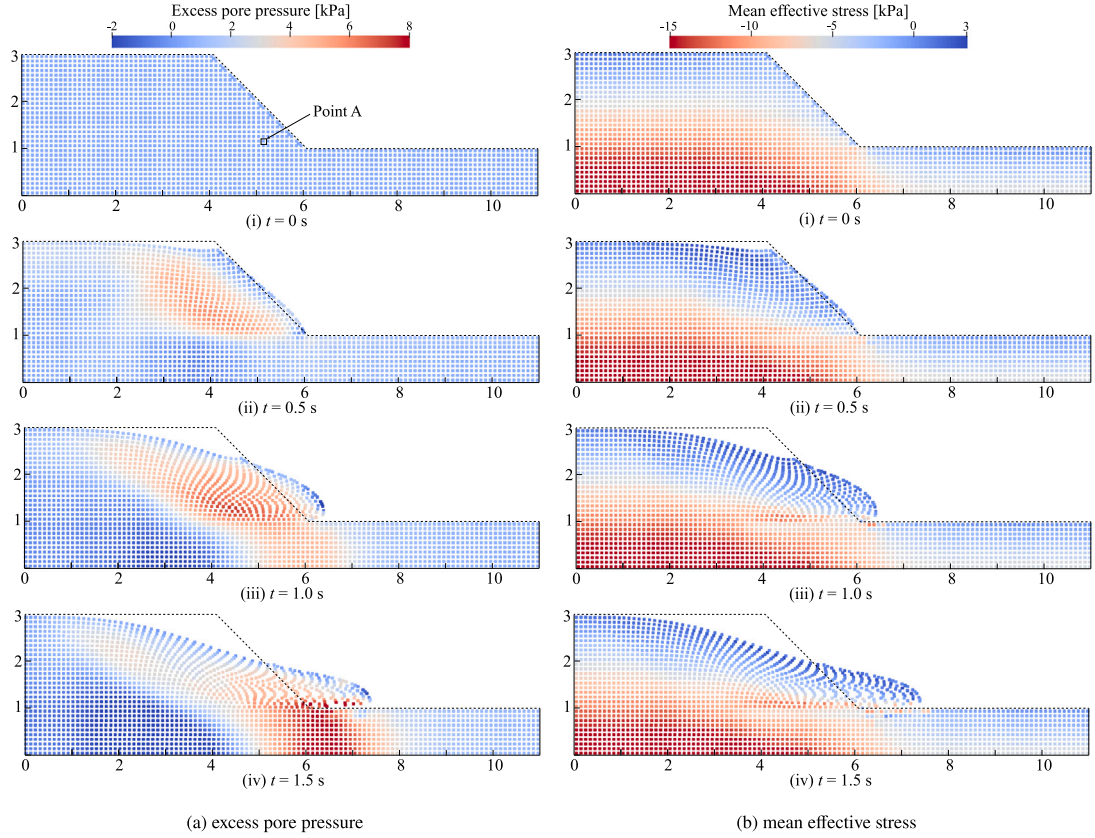


**Fig. 12.** Time evolution of excess pore pressure and mean effective stress during slope failure in water-saturated sand. Results obtained with soil permeability $k = 1.0 \times 10^{-4}$ m/s and initial dilatancy angle $\psi_{ini} = -5°$.

and pore water pressure. In particular, as failure develops, positive (compressive) excess pore pressures build up where high deviatoric plastic straining takes place, which is consistent with the choice of a negative dilation angle for the soil. The excess pore pressure begins to gradually dissipate after about 1.25 s, i.e., as the slope gradually approaches its final equilibrium configuration.

To appreciate the influence of soil permeability on the results of the coupled analysis, the final configuration of the slope at $t = 50.0$ s is shown in Fig. 13 for three different $k$ values. As expected, the numerical model captures correctly that larger soil displacements develop at the slope toe as the permeability is reduced. Such an occurrence is clearly due to the build-up of larger pore pressures, and therefore to a more pronounced reduction in mean effective stress and, proportionally, soil shear resistance. On a related note, Fig. 14 displays the time evolution of the excess pore pressure (difference between the current/total pore pressure value and the hydrostatic pore pressure value at the start of simulation) at a point initially located near the slope toe — point A in Fig. 12(a). The figure confirms that larger pore pressure peaks are attained for lower permeability values, with a slower pore pressure dissipation afterwards. The latter is a consequence of the larger drag

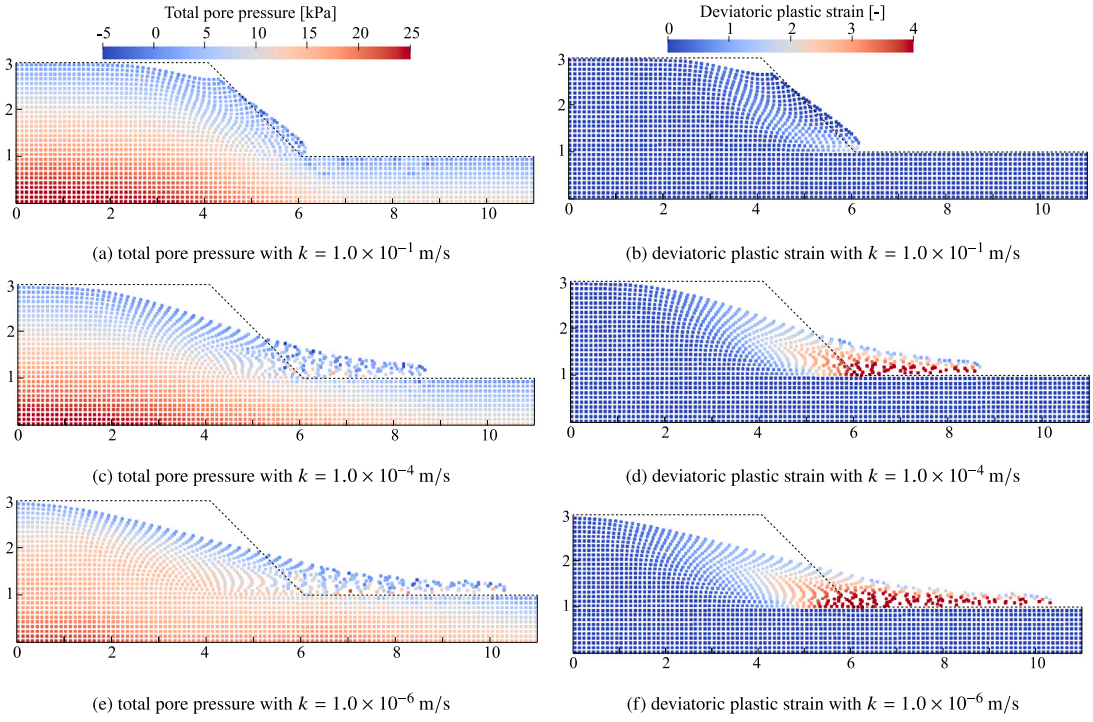


**Fig. 13.** Configuration after slope failure (at $t = 50.0$ s) in water-saturated sand for different values of soil permeability, and associated contours of total pore pressure and deviatoric plastic strain. Results obtained with initial soil dilatancy angle $\psi_{ini} = -5°$.

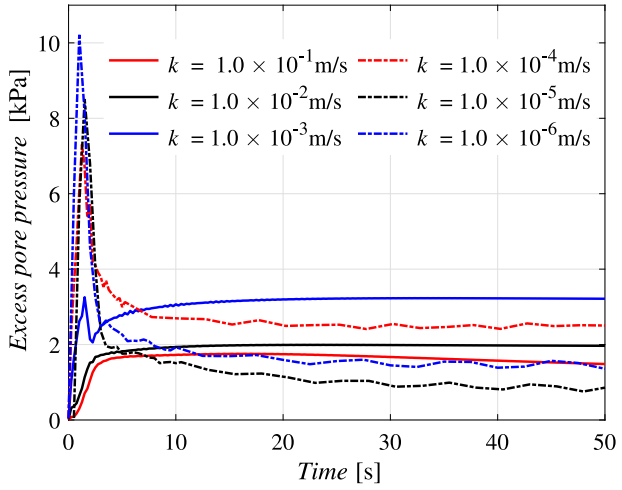


**Fig. 14.** Time evolution of the excess pore pressure at the point A shown in Fig. 12(a) (initially located near the slope toe) for different values of soil permeability. Results obtained with soil initial dilatancy angle $\psi_{ini} = -5°$.

forces $\boldsymbol{R}$ that locally arise with low permeability, which in turn hinders the relative displacement of the soil skeleton and pore water (see Section 2.1). On the other hand, the oscillatory pore pressure dissipation trends obtained for low $k$ values reflect the more pronounced dynamic effects that are associated with a farther/faster soil run-out (Fig. 13).

The impact of the deviatoric–volumetric coupling on soil behaviour is numerically investigated by considering different values of the initial dilation angle ($\psi_{ini}$ in Eq. (17)), namely $-5°$ (contractive soil), $0°$, and $5°$ (dilative soil), in combination with a soil permeability $k = 1.0 \times 10^{-4}$ m/s. The distributions of the total displacement and the deviatoric plastic strain at the end of the simulation ($t = 50.0$ s) are shown in Fig. 15. It is evident that the slope toe undergoes rather limited displacement when dilative soil behaviour is considered, whereas considerable slope deformation takes place in the case of a contractive soil. Such occurrences mainly stem from the fact that much larger positive excess pore pressures build up when the soil is contractive, which can lead to a significant reduction in the mean effective stress across the soil domain, and therefore to a lower resistance to shear loading. In contrast, negative excess pore pressures result during the deviatoric plastic straining of a dilative soil, which ultimately limits the deformations experienced by the slope as a consequence of an enhanced resistance to shear. These observations are further supported by the excess pore pressure curves plotted in Fig. 16 for the same point A (near the slope toe) as indicated in Fig. 12(a). The figure confirms the qualitative expectations about the relationship between the value of $\psi_{ini}$ and the sign of the resulting excess pore pressure (Navas et al., 2018).

### 4.3. Bearing capacity of a strip footing near a slope

As a final application example, the implicit $\overline{\text{B}}$ GIMP-patch method is used to analyse the bearing capacity of a rough strip footing near the crest of a cohesive–frictional, water-saturated slope. The computational model and the associated boundary conditions are displayed in Fig. 17. The slope comprises two layers of fluid-saturated soil; $B = 1.0$ m is the breadth of the foundation, while $\lambda \cdot B$ denotes the distance between the footing edge and the slope crest. The relevant domain dimensions in Fig. 17 are $w_1 = 13.0\,B$, $w_2 = 5.0\,B$, $w_3 = 8.0\,B$, $h_1 = 5.0\,B$, and $h_2 = 1.0\,B$ – note that the rather large $w_1$ has been chosen to avoid boundary effects for all the values of $\lambda \cdot B$ considered in the following. The strip footing has been modelled as a stiff elastic block with a Young's modulus $E_f = 10\,000$ kPa and a Poisson's ratio $\nu_f = 0.3$, while the Mohr–Coulomb parameters of the soil are listed in Table 4. Numerical simulations have been performed using a time step size of $\Delta t = 5 \times 10^{-2}$ s and a loading rate of 20.0 kPa/s. Both the footing and the soil base have been discretised through 4-node quadrilateral grid cells of size 0.5 m × 0.5 m, with each cell initially hosting 2 × 2 equally-spaced MPs. The main purpose of this example case is to demonstrate the suitability of the proposed $\overline{\text{B}}$ GIMP-patch method to study the

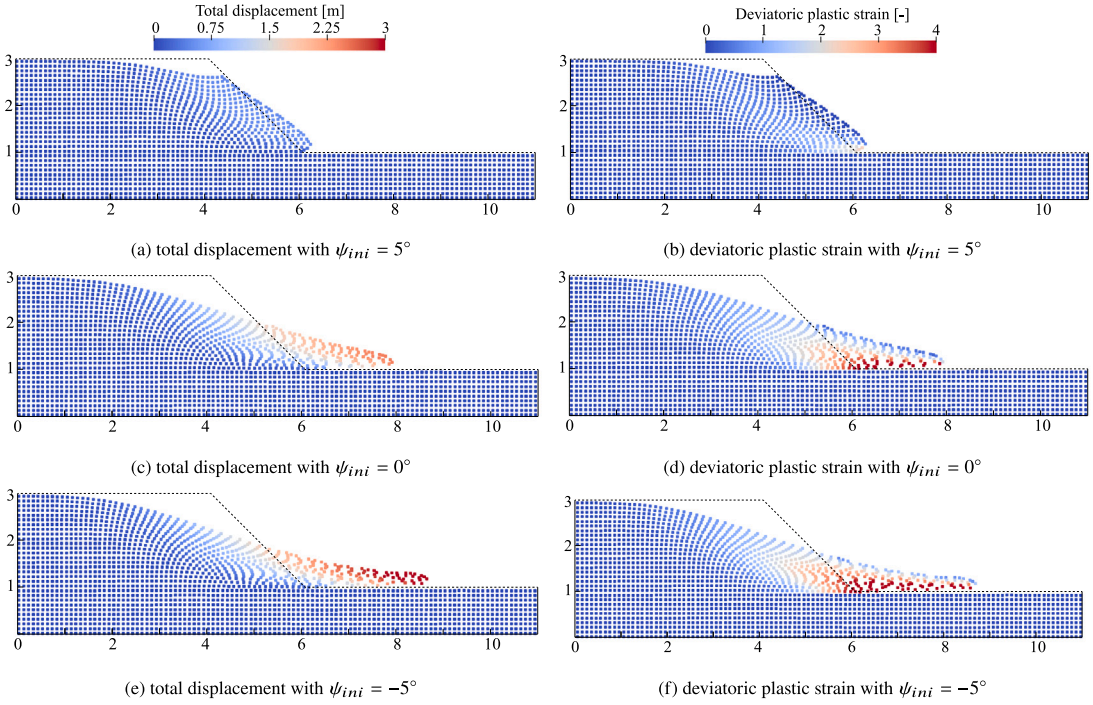


**Fig. 15.** Configuration after slope failure (at $t = 50.0$ s) in water-saturated sand for different values of the initial soil dilatancy angle $\psi_{ini}$, and associated contours of total displacement and deviatoric plastic strain. Results obtained with soil permeability $k = 1.0 \times 10^{-4}$ m/s.

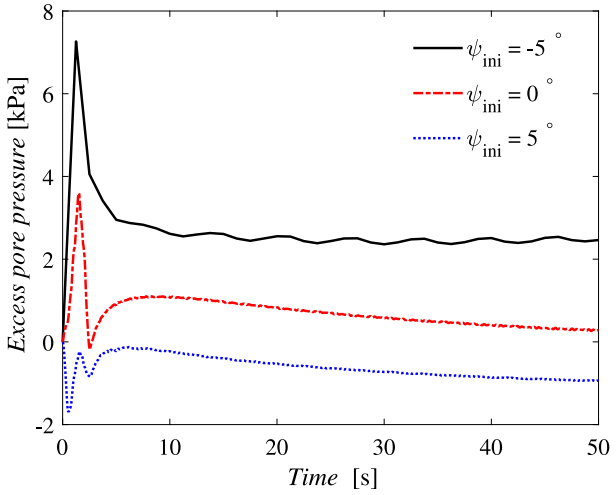


**Fig. 16.** Time evolution of the excess pore pressure at the same point A indicated in Fig. 12(a) (initially located near the slope toe) for different values of the initial soil dilatancy angle $\psi_{ini}$. Results obtained with soil permeability $k = 1.0 \times 10^{-4}$ m/s.

interplay between the foundation failure and slope collapse mechanism as a function of the footing-to-crest distance.

Fig. 18 shows how the footing-to-crest distance factor $\lambda$ affects the large-deformation response of the foundation under the vertical pressure $q$. The distance between the footing edge and the slope crest has a significant influence on the bearing capacity, which tends to increase for larger values of $\lambda$ and converge to the case of a foundation on level ground with no slope — see the strong similarity of the responses associated with $\lambda = 6$ and $\lambda = \infty$. The influence of the footing-to-crest distance becomes gradually more evident as the foundation response enters the large-deformation regime, i.e., after a displacement of about $0.1B$. The lack of a well-defined capacity plateau may be due to concurrent factors that gradually manifest themselves as large

**Table 4**
Soil properties associated with the footing–slope interaction problem in Fig. 17.

| Property | Symbol | Unit | Upper layer | Lower layer |
|---|---|---|---|---|
| Young's modulus | $E$ | [kPa] | 1000 | 1000 |
| Poisson's ratio | $\nu$ | [–] | 0.3 | 0.3 |
| Soil grain density | $\rho_s$ | [kg/m$^3$] | 2650 | 2650 |
| Water density | $\rho_w$ | [kg/m$^3$] | 1000 | 1000 |
| Friction angle | $\phi$ | [°] | 25 | 25 |
| Initial dilation angle | $\psi_{ini}$ | [°] | −5 | −5 |
| Critical dilation angle | $\psi_r$ | [°] | 0 | 0 |
| Dilation evolution parameter | $\eta$ | [–] | −25.0 | −25.0 |
| Cohesion | $c$ | [kPa] | 20.0 | 50.0 |
| Initial porosity | $n$ | [–] | 0.4 | 0.4 |
| Water bulk modulus | $K_w$ | [kPa] | $2.2 \times 10^6$ | $2.2 \times 10^6$ |
| Soil grain bulk modulus | $K_s$ | [kPa] | $1.0 \times 10^{10}$ | $1.0 \times 10^{10}$ |
| Permeability | $k$ | [m/s] | $1.0 \times 10^{-4}$ | $1.0 \times 10^{-4}$ |

foundation settlement takes place. Such factors include (i) the growing contribution to the total capacity offered by the lower soil layer with larger cohesion (see Table 4), as well as (ii) the increase in lateral surcharge, which results in enhanced overburden and confinement. These phenomena are reproduced owing to the large-deformation nature of the performed MPM simulations, and are quantitatively impacted by the specific setting of soil's dilatancy properties.

Fig. 19 shows contours of excess pore pressure and deviatoric plastic strain associated with a foundation displacement equal to $2B$ and different values of $\lambda$. As expected, the largest pore pressure values emerge in the vicinity of the footing, though with a smaller magnitude as $\lambda$ decreases and more effective water drainage through the slope surface occurs. $\lambda$ also affects the type of governing failure mechanisms. For a small footing-to-crest distance (e.g., $\lambda = 0 - 2$ in Fig. 19), the failure mechanism is dominated by the development of a shear band through the slope, that is from the footing to the slope toe — as a consequence, the footing experiences a significant in-plane rotation during its collapse. In contrast, larger $\lambda$ values determine a decreasing influence of the slope, so that a clear vertical foundation failure is first observed prior to a general sideways displacement of the soil towards the slope.

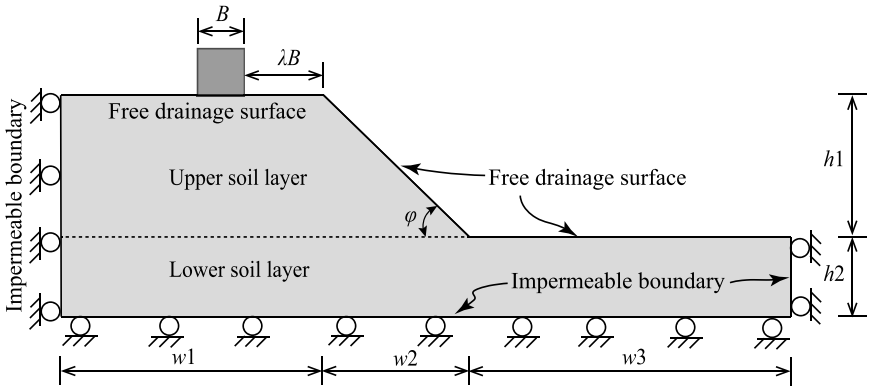


**Fig. 17.** Reference footing–slope interaction problem: computational domain and boundary conditions (not to scale).

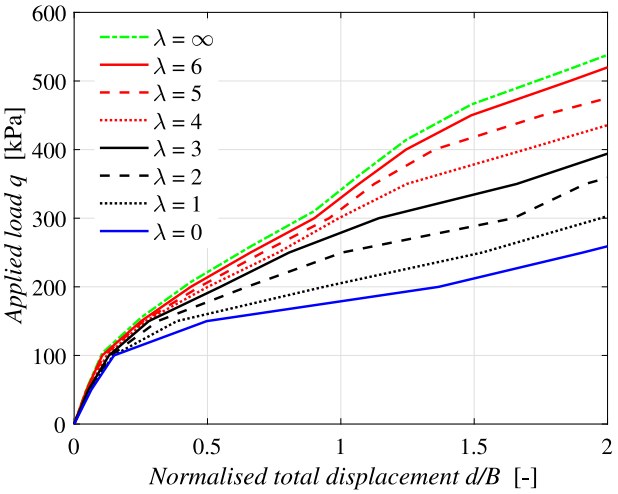


**Fig. 18.** Influence of the footing-to-crest distance on the large-deformation load–displacement response of the foundation in Fig. 17.

## 5. Conclusion

This paper has presented a numerical method for the analysis of large-deformation hydro-mechanical problems in fluid-saturated elasto-plastic geomaterials. The proposed method belongs in the family of MPMs, and involves a combination of the recently proposed implicit GIMP-patch method for poroelastic materials and the $\overline{\mathrm{B}}$ kinematic enhancement against volumetric locking. The need for such an enhancement is motivated by the spurious stress oscillations and excessively stiff responses that are obtained in the absence of specific anti-locking measures, especially when a (nearly) isochoric behaviour of the soil skeleton is considered. Details about the formulation and implementation of the implicit $\overline{\mathrm{B}}$ GIMP-patch method have been provided, starting from a three-field $u$–$p$–$U$ formulation of the coupled hydro-mechanical problem. The proposed $\overline{\mathrm{B}}$ GIMP-patch method has been evaluated through several 2D benchmark problems (footing bearing capacity, slope failure, and footing–slope interaction), and found to be largely satisfactory in terms of accuracy, stability, and anti-locking performance. Further applications to more complex large-deformation coupled problems and soil constitutive relationships, including proper treatment of finite-strain kinematics, will be tackled in future work.

## CRediT authorship contribution statement

**Xiangcou Zheng:** Methodology, Software, Validation, Investigation, Writing – original draft. **Federico Pisanò:** Funding acquisition, Conceptualization, Supervision, Writing – review & editing. **Philip J. Vardon:** Conceptualization, Supervision, Writing – review & editing. **Michael A. Hicks:** Funding acquisition, Conceptualization, Supervision, Writing – review & editing.

## Declaration of competing interest

The authors declare that they have no known competing financial interests or personal relationships that could have appeared to influence the work reported in this paper.

## Acknowledgements

The first author wishes to acknowledge the China Scholarship Council (CSC) and the Geo-Engineering Section of Delft University of Technology, Netherlands for the financial support. The constructive feedback of the anonymous reviewers is also greatly appreciated.

## Appendix. Sub-matrices for the discrete system of governing equations (6)

In the framework of GIMP, the matrices in Eq. (6) are defined for a specific grid cell node $i$ as follows:

$$\mathbf{M}_{u,i} = \sum_{mp=1}^{N_{mp}} \mathbf{S}_{u,i}^{\mathrm{T}}(\boldsymbol{x}_{mp}) m_{u,mp} \mathbf{S}_{u,i}(\boldsymbol{x}_{mp}) = \sum_{mp=1}^{N_{mp}} \mathbf{S}_{u,i}^{\mathrm{T}}(\boldsymbol{x}_{mp})(1-n)\rho_{s,mp} V_{mp} \mathbf{S}_{u,i}(\boldsymbol{x}_{mp}) \tag{A.1a}$$

$$\mathbf{M}_{U,i} = \sum_{mp=1}^{N_{mp}} \mathbf{S}_{U,i}^{\mathrm{T}}(\boldsymbol{x}_{mp}) m_{U,mp} \mathbf{S}_{U,i}(\boldsymbol{x}_{mp}) = \sum_{mp=1}^{N_{mp}} \mathbf{S}_{U,i}^{\mathrm{T}}(\boldsymbol{x}_{mp}) n\rho_{w,mp} V_{mp} \mathbf{S}_{U,i}(\boldsymbol{x}_{mp}) \tag{A.1b}$$

$$\mathbf{C}_{1,i} = \sum_{mp=1}^{N_{mp}} \mathbf{S}_{u,i}^{\mathrm{T}}(\boldsymbol{x}_{mp}) n^2 k^{-1} \mathbf{S}_{u,i}(\boldsymbol{x}_{mp}) V_{mp} \tag{A.1c}$$

$$\mathbf{C}_{2,i} = \sum_{mp=1}^{N_{mp}} \mathbf{S}_{u,i}^{\mathrm{T}}(\boldsymbol{x}_{mp}) n^2 k^{-1} \mathbf{S}_{U,i}(\boldsymbol{x}_{mp}) V_{mp} \tag{A.1d}$$

$$\mathbf{C}_{3,i} = \sum_{mp=1}^{N_{mp}} \mathbf{S}_{U,i}^{\mathrm{T}}(\boldsymbol{x}_{mp}) n^2 k^{-1} \mathbf{S}_{U,i}(\boldsymbol{x}_{mp}) V_{mp} \tag{A.1e}$$

$$\mathbf{K}_{u,i} = \sum_{mp=1}^{N_{mp}} \nabla \mathbf{S}_{u,i}^{\mathrm{T}}(\boldsymbol{x}_{mp}) \mathbf{D}^{e} \nabla \mathbf{S}_{u,i}(\boldsymbol{x}_{mp}) V_{mp} = \sum_{mp=1}^{N_{mp}} \overline{\mathbf{B}}_{u,i}^{\mathrm{T}}(\boldsymbol{x}_{mp}) \mathbf{D}^{e} \overline{\mathbf{B}}_{u,i}(\boldsymbol{x}_{mp}) V_{mp} \tag{A.1f}$$

$$\mathbf{G}_{1,i} = \sum_{mp=1}^{N_{mp}} \nabla \mathbf{S}_{u,i}^{\mathrm{T}}(\boldsymbol{x}_{mp}) \boldsymbol{m}(1-n) S_{p,i}(\boldsymbol{x}_{mp}) V_{mp}$$
$$= \sum_{mp=1}^{N_{mp}} \overline{\mathbf{B}}_{u,i}^{\mathrm{T}}(\boldsymbol{x}_{mp}) \boldsymbol{m}(1-n) S_{p,i}(\boldsymbol{x}_{mp}) V_{mp} \tag{A.1g}$$

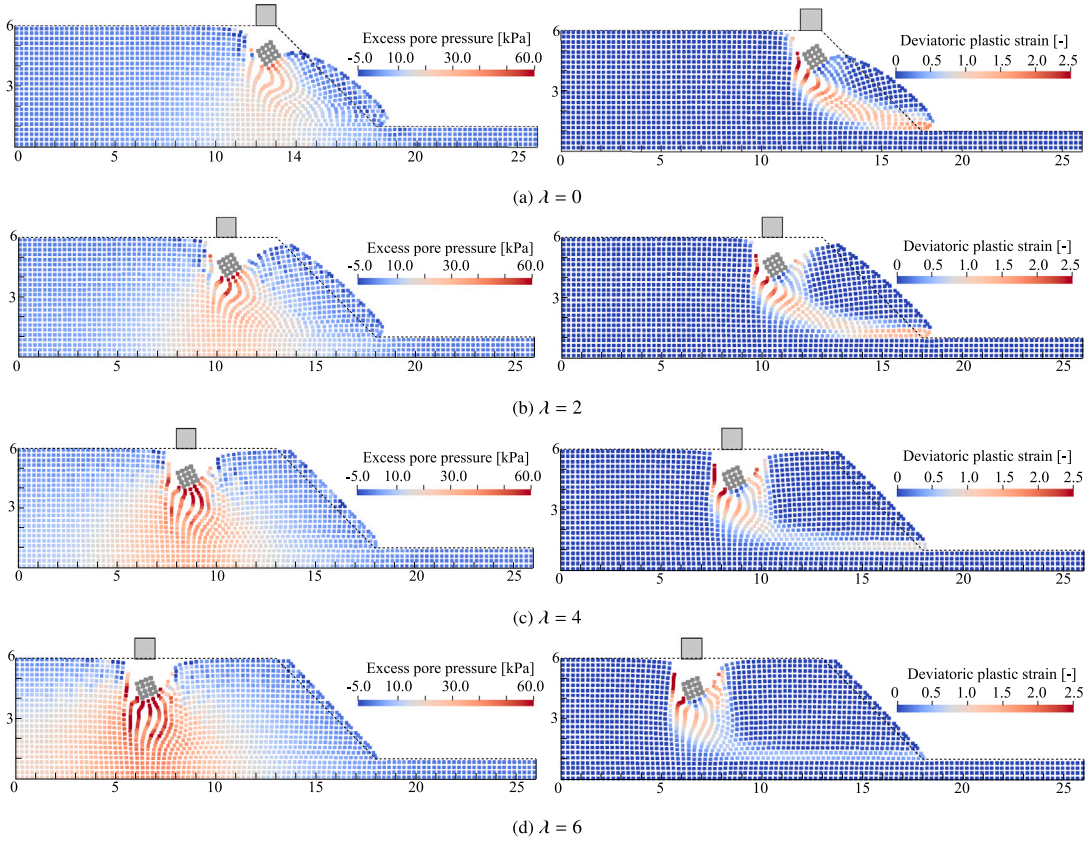


**Fig. 19.** Final excess pore pressure (left) and deviatoric plastic strain (right) distributions associated with the footing–slope interaction problem in Fig. 17. Results obtained with soil permeability $k = 1.0 \times 10^{-4}$ m/s at a total footing displacement equal to $2B$.

$$\mathbf{G}_{2,i} = \sum_{mp=1}^{N_{mp}} \nabla \mathbf{S}_{U,i}^{\mathrm{T}}(\boldsymbol{x}_{mp}) \boldsymbol{m} n S_{p,i}(\boldsymbol{x}_{mp}) V_{mp} = \sum_{mp=1}^{N_{mp}} \overline{\mathbf{B}}_{U,i}^{\mathrm{T}}(\boldsymbol{x}_{mp}) \boldsymbol{m} n S_{p,i}(\boldsymbol{x}_{mp}) V_{mp} \tag{A.1h}$$

$$P_i = \sum_{mp=1}^{N_{mp}} S_{p,i}^{\mathrm{T}}(\boldsymbol{x}_{mp}) \frac{1}{Q} S_{p,i}(\boldsymbol{x}_{mp}) V_{mp} \tag{A.1i}$$

where the subscript $i$ defines the $i$th grid cell node; subscripts $u$ and $s$ define the values related to the soil phase, while subscripts $U$ and $w$ define the values related to the water phase; $\boldsymbol{x}_{mp}$ are the coordinates of the MPs; $N_{mp}$ is the total number of MPs; $\mathbf{M}_u$ and $\mathbf{M}_U$ are mass matrices for the soil and water phases; $\mathbf{C}_1$, $\mathbf{C}_2$ and $\mathbf{C}_3$ are damping matrices physically associated with the grain–fluid drag; $\mathbf{K}_u$ is the stiffness matrix of the solid skeleton; $\mathbf{P}$ is a compressibility matrix determined by the bulk stiffness of the solid grains and pore water; and $\mathbf{G}_1$ and $\mathbf{G}_2$ are matrices describing the hydro-mechanical coupling between the skeleton deformation and pore water flow.

Similarly, the external force vectors in Eq. (6) are re-written as

$$\bar{\boldsymbol{f}}_{s,i} = \sum_{mp=1}^{N_{bmp}} \mathbf{S}_{u,i}^{\mathrm{T}}(\boldsymbol{x}_{mp}) \bar{\boldsymbol{\tau}}(t) + \sum_{mp=1}^{N_{bmp}} \mathbf{S}_{u,i}^{\mathrm{T}}(\boldsymbol{x}_{mp}) m_{u,mp} \boldsymbol{b} \tag{A.2a}$$

$$\bar{\boldsymbol{f}}_{w,i} = \sum_{mp=1}^{N_{bmp}} \mathbf{S}_{u,i}^{\mathrm{T}}(\boldsymbol{x}_{mp}) m_{U,mp} \boldsymbol{b} \tag{A.2b}$$

where $\bar{\boldsymbol{f}}_s$ and $\bar{\boldsymbol{f}}_w$ are nodal force vectors associated with the solid and water phases, $\bar{\boldsymbol{\tau}}(t)$ is the prescribed surface traction, $\boldsymbol{b}$ is the body force, and $N_{bmp}$ is the total number of boundary MPs.

## References


Abe, K., Soga, K., Bandara, S., 2014. Material point method for coupled hydromechanical problems. J. Geotech. Geoenviron. Eng. 140 (3), 04013033.

Bandara, S., Soga, K., 2015. Coupling of soil deformation and pore fluid flow using material point method. Comput. Geotech. 63, 199–214.

Bardenhagen, S.G., Kober, E.M., 2004. The generalized interpolation material point method. Comput. Model. Eng. Sci. 5 (6), 477–496.

Bisht, V., Salgado, R., Prezzi, M., 2021. Simulating penetration problems in incompressible materials using the material point method. Comput. Geotech. 133, 103593.

Ceccato, F., Beuth, L., Vermeer, P.A., Simonini, P., 2016. Two-phase material point method applied to the study of cone penetration. Comput. Geotech. 80, 440–452.

Charlton, T.J., 2018. An Implicit Generalised Interpolation Material Point Method for Large Deformation and Gradient Elasto-Plasticity (Ph.D. thesis). Durham University.

Coombs, W.M., Augarde, C.E., Brennan, A.J., Brown, M.J., Charlton, T.J., Knappett, J.A., Motlagh, Y.G., Wang, L., 2020. On Lagrangian mechanics and the implicit material point method for large deformation elasto-plasticity. Comput. Methods Appl. Mech. Engrg. 358, 112622.

Coombs, W.M., Charlton, T.J., Cortis, M., Augarde, C.E., 2018. Overcoming volumetric locking in material point methods. Comput. Methods Appl. Mech. Engrg. 333, 1–21.

Cuomo, S., Perna, A.D., Martinelli, M., 2021. Material point method (MPM) hydro-mechanical modelling of flows impacting rigid walls. Can. Geotech. J. 58 (11), 1730–1743.

Da Silva, M., Krabbenhoft, K., Lyamin, A., Sloan, S., 2011. Rigid-plastic large-deformation analysis of geotechnical penetration problems. Proceedings of the 13th IACMAG conference. Computer methods for geomechanics: frontiers and new applications 1, 42–47.

González Acosta, L.J., Vardon, P.J., Hicks, M.A., 2017. Composite material point method (CMPM) to improve stress recovery for quasi-static problems. Procedia Eng. 175, 324–331.

González Acosta, L.J., Vardon, P.J., Hicks, M.A., 2021. Development of an implicit contact technique for the material point method. Comput. Geotech. 130, 103859.

González Acosta, L.J., Vardon, P.J., Remmerswaal, G., Hicks, M.A., 2020. An investigation of stress inaccuracies and proposed solution in the material point method. Comput. Mech. 65 (2), 555–581.

González Acosta, L.J., Zheng, X.C., Vardon, P.J., Hicks, M.A., Pisanò, F., 2019. On stress oscillation in MPM simulations involving one or two phases. In: MPM 2019: 2nd International Conference on the Material Point Method for Modelling Soil–Water–Structure Interaction.

Higo, Y., Nishimura, D., Oka, F., 2015. Dynamic analysis of unsaturated embankment considering the seepage flow by a GIMP-FDM coupled method. In: Proceedings

of the 14th International Conference of International Association for Computer Methods and Recent Advances in Geomechanics, 2014. IACMAG 2014, Taylor & Francis Books Ltd, pp. 1761–1766.
Higo, Y., Oka, F., Kimoto, S., Morinaka, Y., Goto, Y., Chen, Z., 2010. A coupled MPM-FDM analysis method for multi-phase elasto-plastic soils. Soils Found. 50 (4), 515–532.
Holzapfel, A.G., 2000. Nonlinear Solid Mechanics II. Wiley, New York.
Hughes, T.J., 1980. Generalization of selective integration procedures to anisotropic and nonlinear media. Internat. J. Numer. Methods Engrg. 15 (9), 1413–1418.
Hughes, T.J., 1987. The Finite Element Method: Linear Static and Dynamic Finite Element Analysis. Prentice-Hall.
Iaconeta, I., Larese, A., Rossi, R., Oñate, E., 2019. A stabilized mixed implicit material point method for non-linear incompressible solid mechanics. Comput. Mech. 63 (6), 1243–1260.
Jassim, I., Stolle, D., Vermeer, P., 2013. Two-phase dynamic analysis by material point method. Int. J. Numer. Anal. Methods Geomech. 37 (15), 2502–2522.
Kiriyama, T., Higo, Y., 2020. Arbitrary particle domain interpolation method and application to problems of geomaterial deformation. Soils Found. 60 (6), 1422–1439.
Kularathna, S., Liang, W., Zhao, T., Chandra, B., Zhao, J., Soga, K., 2021. A semi-implicit material point method based on fractional-step method for saturated soil. Int. J. Numer. Anal. Methods Geomech. 45 (10), 1405–1436.
Kularathna, S., Soga, K., 2017. Implicit formulation of material point method for analysis of incompressible materials. Comput. Methods Appl. Mech. Engrg. 313, 673–686.
Lee, N.-S., Bathe, K.-J., 1993. Effects of element distortions on the performance of isoparametric elements. Internat. J. Numer. Methods Engrg. 36 (20), 3553–3576.
Lei, X., He, S., Abed, A., Chen, X., Yang, Z., Wu, Y., 2021a. A generalized interpolation material point method for modelling coupled thermo-hydro-mechanical problems. Comput. Methods Appl. Mech. Engrg. 386, 114080.
Lei, X., He, S., Wu, L., 2020. Stabilized generalized interpolation material point method for coupled hydro-mechanical problems. Comput. Part. Mech. 1–20.
Lei, X., He, S., Wu, L., 2021b. Stabilized generalized interpolation material point method for coupled hydro-mechanical problems. Comput. Part. Mech. 8 (4), 701–720.
Liu, C.Q., Sun, Q.C., Jin, F., Zhou, G.G., 2017. A fully coupled hydro-mechanical material point method for saturated dense granular materials. Powder Technol. 314, 110–120.
Martinelli, M., Galavi, V., 2022. An explicit coupled MPM formulation to simulate penetration problems in soils using quadrilateral elements. Comput. Geotech. 145, 104697.
Martinelli, M., Pisanò, F., 2022. Relating cone penetration resistance to sand state through material point method large-deformation modelling. Géotechnique Lett. 1–22.
Martinelli, M., Rohe, A., 2015. Modelling fluidisation and sedimentation using material point method. In: 1st Pan-American Congress on Computational Mechanics. pp. 1–12.
Mast, C., Mackenzie-Helnwein, P., Arduino, P., Miller, G.R., Shin, W., 2012. Mitigating kinematic locking in the material point method. J. Comput. Phys. 231 (16), 5351–5373.
Navas, P., Sanavia, L., López-Querol, S., Rena, C.Y., 2018. u–w formulation for dynamic problems in large deformation regime solved through an implicit meshfree scheme. Comput. Mech. 62 (4), 745–760.
Nazem, M., Carter, J.P., Sheng, D., Sloan, S.W., 2009. Alternative stress-integration schemes for large-deformation problems of solid mechanics. Finite Elem. Anal. Des. 45 (12), 934–943.
Nazem, M., Sheng, D., Carter, J.P., 2006. Stress integration and mesh refinement for large deformation in geomechanics. Internat. J. Numer. Methods Engrg. 65 (7), 1002–1027.
Newmark, N.M., 1959. A method of computation for structural dynamics. J. Eng. Mech. Div. 85 (3), 67–94.
Rajendran, S., 2010. A technique to develop mesh-distortion immune finite elements. Comput. Methods Appl. Mech. Engrg. 199 (17–20), 1044–1063.
Sadeghirad, A., Brannon, R.M., Burghardt, J., 2011. A convected particle domain interpolation technique to extend applicability of the material point method for problems involving massive deformations. Internat. J. Numer. Methods Engrg. 86 (12), 1435–1456.
Soga, K., Alonso, E., Yerro, A., Kumar, K., Bandara, S., 2015. Trends in large-deformation analysis of landslide mass movements with particular emphasis on the material point method. Géotechnique 66 (3), 248–273.
Sołowski, W., Sloan, S., 2015. Evaluation of material point method for use in geotechnics. Int. J. Numer. Anal. Methods Geomech. 39 (7), 685–701.
Steffen, M., Kirby, R.M., Berzins, M., 2008. Analysis and reduction of quadrature errors in the material point method (MPM). Internat. J. Numer. Methods Engrg. 76 (6), 922–948.
Tran, Q.-A., Sołowski, W., 2019. Temporal and null-space filter for the material point method. Internat. J. Numer. Methods Engrg. 120 (3), 328–360.
Wang, D., Bienen, B., Nazem, M., Tian, Y., Zheng, J., Pucker, T., Randolph, M.F., 2015. Large deformation finite element analyses in geotechnical engineering. Comput. Geotech. 65, 104–114.
Wang, B., Vardon, P.J., Hicks, M.A., 2018. Rainfall-induced slope collapse with coupled material point method. Eng. Geol. 239, 1–12.
Woo, S.I., Salgado, R., 2018. Simulation of penetration of a foundation element in tresca soil using the generalized interpolation material point method (GIMP). Comput. Geotech. 94, 106–117.
Yang, Y., Sun, P., Chen, Z., 2017. Combined MPM-DEM for simulating the interaction between solid elements and fluid particles. Commun. Comput. Phys. 21 (5), 1258–1281.
Yerro, A., Alonso, E., Pinyol, N., 2015. The material point method for unsaturated soils. Géotechnique 65 (3), 201–217.
Yerro, A., Rohe, A., Soga, K., 2017. Modelling internal erosion with the material point method. Procedia Eng. 175, 365–372.
Yuan, W.H., Wang, H.C., Liu, K., Zhang, W., Wang, D., Wang, Y., 2021. Analysis of large deformation geotechnical problems using implicit generalized interpolation material point method. J. Zhejiang Univ. Sci. A 22 (11), 909–923.
Zabala, F., Alonso, E., 2011. Progressive failure of aznalcóllar dam using the material point method. Géotechnique 61 (9), 795–808.
Zhang, D.Z., Ma, X., Giguere, P.T., 2011. Material point method enhanced by modified gradient of shape function. J. Comput. Phys. 230 (16), 6379–6398.
Zhang, H.W., Wang, K.P., Chen, Z., 2009. Material point method for dynamic analysis of saturated porous media under external contact/impact of solid bodies. Comput. Methods Appl. Mech. Engrg. 198 (17–20), 1456–1472.
Zhang, H.W., Wang, K.P., Zhang, Z., 2007. Material point method for numerical simulation of failure phenomena in multiphase porous media. In: Computational Mechanics: International Symposium on Computational Mechanics. Springer, pp. 36–47.
Zhang, F., Zhang, X., Sze, K.Y., Lian, Y., Liu, Y., 2017. Incompressible material point method for free surface flow. J. Comput. Phys. 330, 92–110.
Zhao, Y., Choo, J., 2020. Stabilized material point methods for coupled large deformation and fluid flow in porous materials. Comput. Methods Appl. Mech. Engrg. 362, 112742.
Zheng, Y.G., Gao, F., Zhang, H.W., Lu, M.K., 2013. Improved convected particle domain interpolation method for coupled dynamic analysis of fully saturated porous media involving large deformation. Comput. Methods Appl. Mech. Engrg. 257, 150–163.
Zheng, X., Pisanò, F., Vardon, P.J., Hicks, M.A., 2021a. An explicit stabilised material point method for coupled hydromechanical problems in two-phase porous media. Comput. Geotech. 135, 104112.
Zheng, X., Pisanò, F., Vardon, P.J., Hicks, M.A., 2021b. Fully implicit, stabilised, three-field material point method for dynamic coupled problems. Eng. Comput. (submitted for publication).
Zienkiewicz, O.C., Chan, A., Pastor, M., Schrefler, B., Shiomi, T., 1999. Computational Geomechanics with Special Reference to Earthquake Engineering. John Wiley & Sons.
Zienkiewicz, O., Chang, C., Bettess, P., 1980. Drained, undrained, consolidating and dynamic behaviour assumptions in soils. Géotechnique 30 (4), 385–395.
Zienkiewicz, O., Shiomi, T., 1984. Dynamic behaviour of saturated porous media; the generalized Biot formulation and its numerical solution. Int. J. Numer. Anal. Methods Geomech. 8 (1), 71–96.
Zienkiewicz, O.C., Taylor, R.L., Zhu, J.Z., 2005. The Finite Element Method: Its Basis and Fundamentals. Elsevier.
Zienkiewicz, O.C., Zhu, J., 1992. The superconvergent patch recovery (SPR) and adaptive finite element refinement. Comput. Methods Appl. Mech. Engrg. 101 (1–3), 207–224.